

Supplementary Materials for

Ordered colloidal clusters constructed by nanocrystals with valence for efficient CO₂ photoreduction

Jianwei Nai, Sibow Wang, Xiong Wen (David) Lou*

*Corresponding author. Email: xwlou@ntu.edu.sg

Published 13 December 2019, *Sci. Adv.* 5, eaax5095 (2019)

DOI: 10.1126/sciadv.aax5095

This PDF file includes:

- Fig. S1. Characterization of Co-Fe PBA CC-1.
- Fig. S2. The molecular framework of the Co-Fe PBA materials.
- Fig. S3. FESEM overview image of Co-Fe PBA CC-1.
- Fig. S4. Characterization of Co-Fe PBA CC-2.
- Fig. S5. FESEM overview image of Co-Fe PBA CC-2.
- Fig. S6. Schematic models of Co-Fe PBA CC-2.
- Fig. S7. TEM characterization of Co-Fe PBA CC-2.
- Fig. S8. SAXS data of the samples.
- Fig. S9. FESEM and TEM images of the intermediate products for the synthesis of Co-Fe PBA CC-1.
- Fig. S10. XRD patterns of different products.
- Fig. S11. EDX spectrum of the nanocubes.
- Fig. S12. FTIR spectra of different samples.
- Fig. S13. FESEM images of the control samples with different amounts of SDS.
- Fig. S14. FESEM images of the intermediate products for the synthesis of the sample with the absence of SDS (as seen in fig. S13A).
- Fig. S15. FESEM images of the control samples with different surfactants.
- Fig. S16. TEM and SAED images of a typical core@satellite superstructure obtained at the reaction time of 45 min for the synthesis of Co-Fe PBA CC-1.
- Fig. S17. Characterization of a typical Co-Fe PBA CC-1 particle.
- Fig. S18. Characterization of some isolated SNCs that fall off the core at the reaction time of 1 hour for the synthesis of Co-Fe PBA CC-1.
- Fig. S19. TEM images of the typical particle obtained at different reaction times for the synthesis of Co-Fe PBA CC-1.
- Fig. S20. TEM images of some occasionally observed particles in the sample of Co-Fe PBA CC-1.
- Fig. S21. FESEM images of the intermediate products for the synthesis of Co-Fe PBA CC-2.

Fig. S22. Characterization of the core@satellite superstructures obtained at the reaction time of 45 min for the synthesis of Co-Fe PBA CC-2.

Fig. S23. A FESEM image shows the assembly imperfections in the packing of the core@satellite superstructures.

Fig. S24. XRD patterns of the Co-Fe-O HCCs that derived from the Co-Fe PBA CCs.

Fig. S25. EDX spectra of the Co-Fe-O HCCs derived from the Co-Fe PBA CCs.

Fig. S26. Characterization of Co-Fe-O HCC-1.

Fig. S27. Characterization of Co-Fe-O HCC-2.

Fig. S28. Light absorption spectrum of the Co-Fe PBA CC-1 catalyst.

Fig. S29. Stability tests of the Co-Fe PBA CC-1 catalyst for CO₂ photoreduction.

Fig. S30. Characterizations of the Co-Fe PBA CC-1 catalyst after the photocatalysis.

Fig. S31. Characterization of the Co-Fe PBA CCs after storage as powder in air for more than 6 months.

Fig. S32. Characterization of the Co-Fe PBA NPs as a catalyst without colloidal assembly.

Fig. S33. Electrochemical measurements of the Co-Fe PBA CC-1 catalyst.

Fig. S34. Room temperature PL spectra of the reaction systems with and without the Co-Fe PBA CC-1 catalyst.

Fig. S35. Proposed mechanism for the photocatalytic conversion of CO₂ to CO.

Fig. S36. Liquid chromatography–mass spectrometry analyses of the oxidation species.

Fig. S37. N₂ adsorption measurements of diverse catalysts.

Fig. S38. CO₂ adsorption isotherms of Co-Fe PBA CC-2 and Co-Fe PBA NPs.

Table S1. Some parameters of the Co-Fe PBA CCs.

Table S2. The position of FTIR peaks of the samples and their assignment.

Table S3. Similarities of the entropic and enthalpic valence of NCs and their operations in the assembly.

Table S4. Comparison of the photocatalytic CO₂ reduction performance of the Co-Fe PBA CCs prepared in this work with some recently reported advanced catalysts.

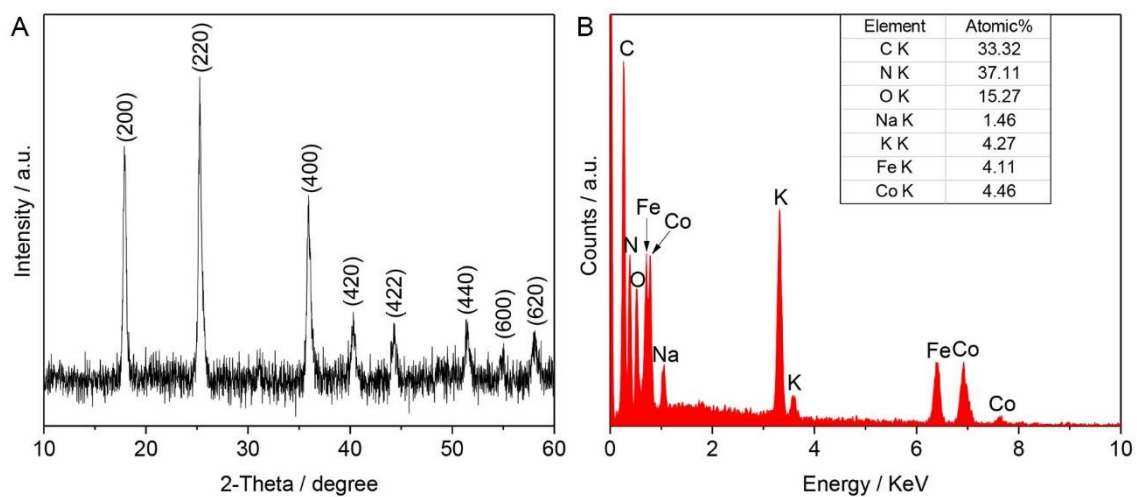


Fig. S1. Characterization of Co-Fe PBA CC-1. (A) XRD pattern. XRD result displays a typical pattern of the face-centered cubic structure of PBAs. (B) EDX spectrum. EDX result indicates the atomic ratio of Na/K/Fe/Co is 0.33:0.96:0.92:1.

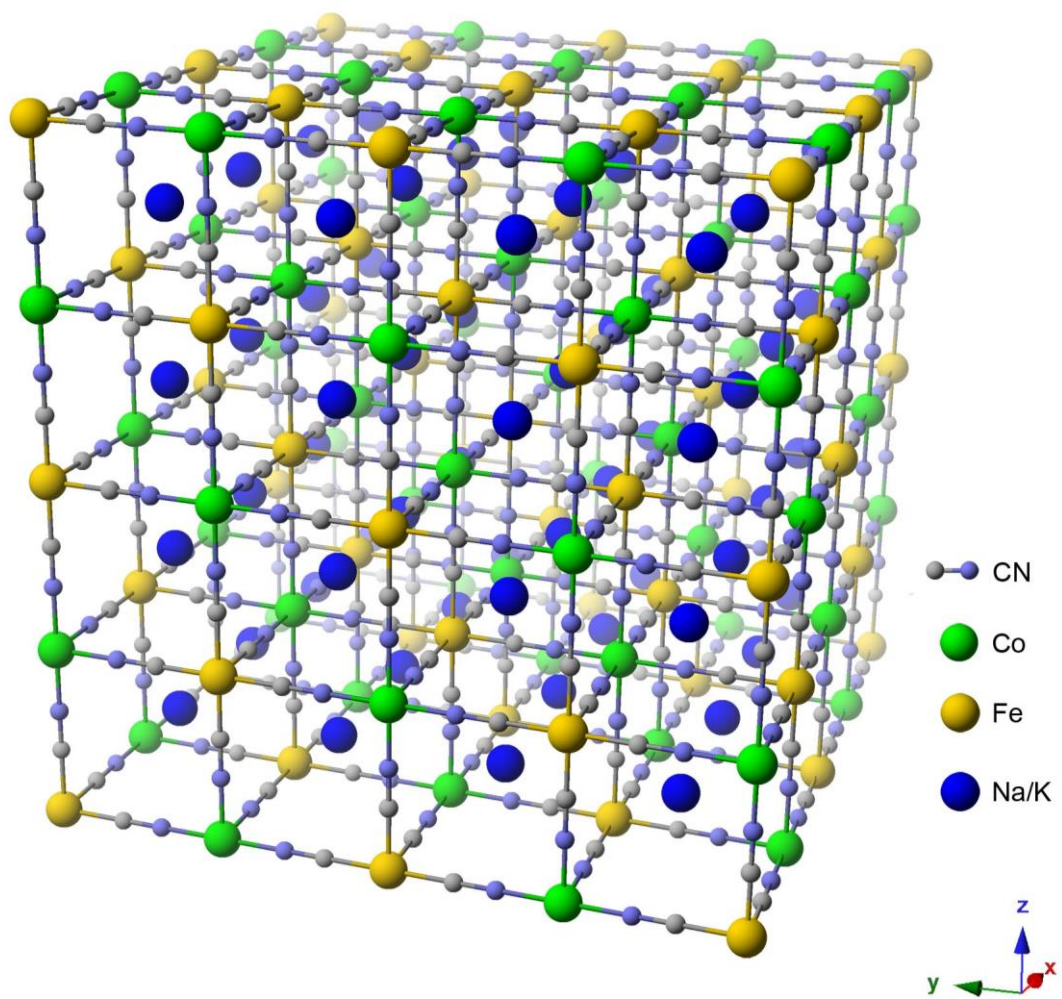


Fig. S2. The molecular framework of the Co-Fe PBA materials. Rich alkali cations can be embedded in the open channels.



Fig. S3. FESEM overview image of Co-Fe PBA CC-1.

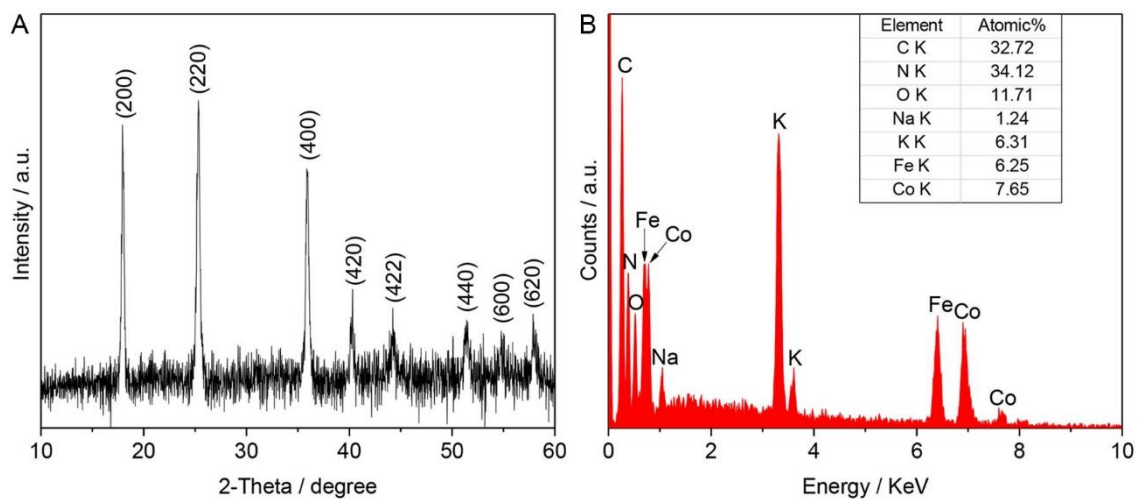


Fig. S4. Characterization of Co-Fe PBA CC-2. (A) XRD pattern. XRD result displays a typical pattern of the face-centered cubic structure of PBAs. (B) EDX spectrum. EDX result indicates the atomic ratio of Na/K/Fe/Co is 0.16:0.82:0.82:1.

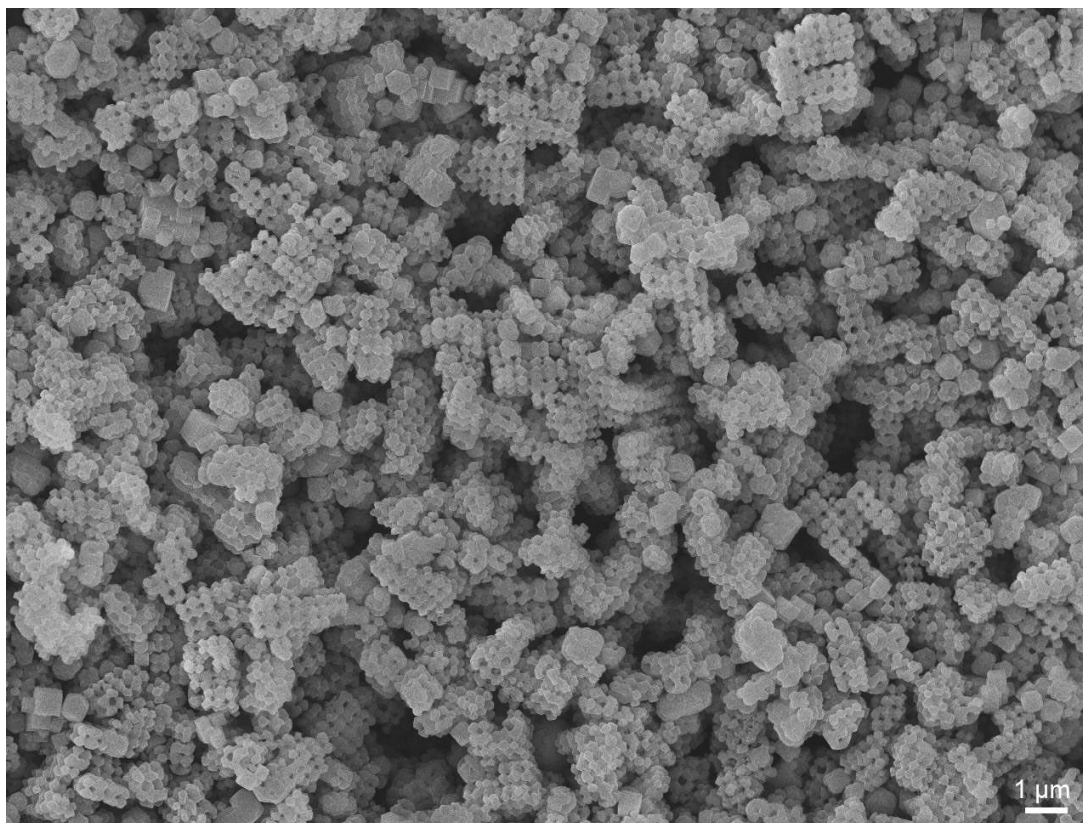


Fig. S5. FESEM overview image of Co-Fe PBA CC-2.

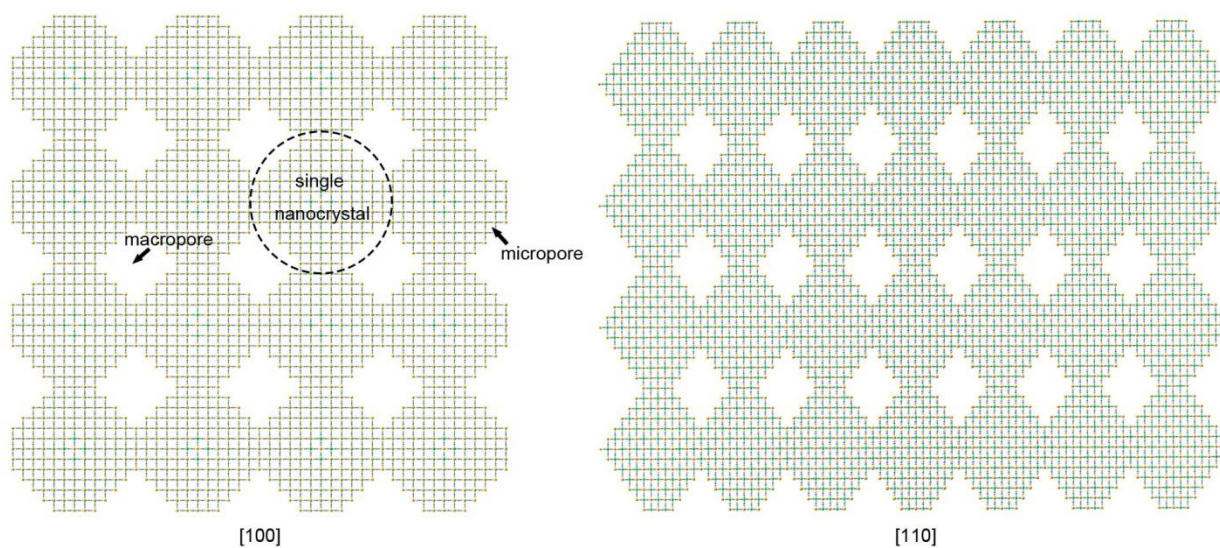


Fig. S6. Schematic models of Co-Fe PBA CC-2. It demonstrates the concept of “multilevel porous” material. Note that the dimensional scale ratio of the micropore/macropore here might not be in line with the practical situation.

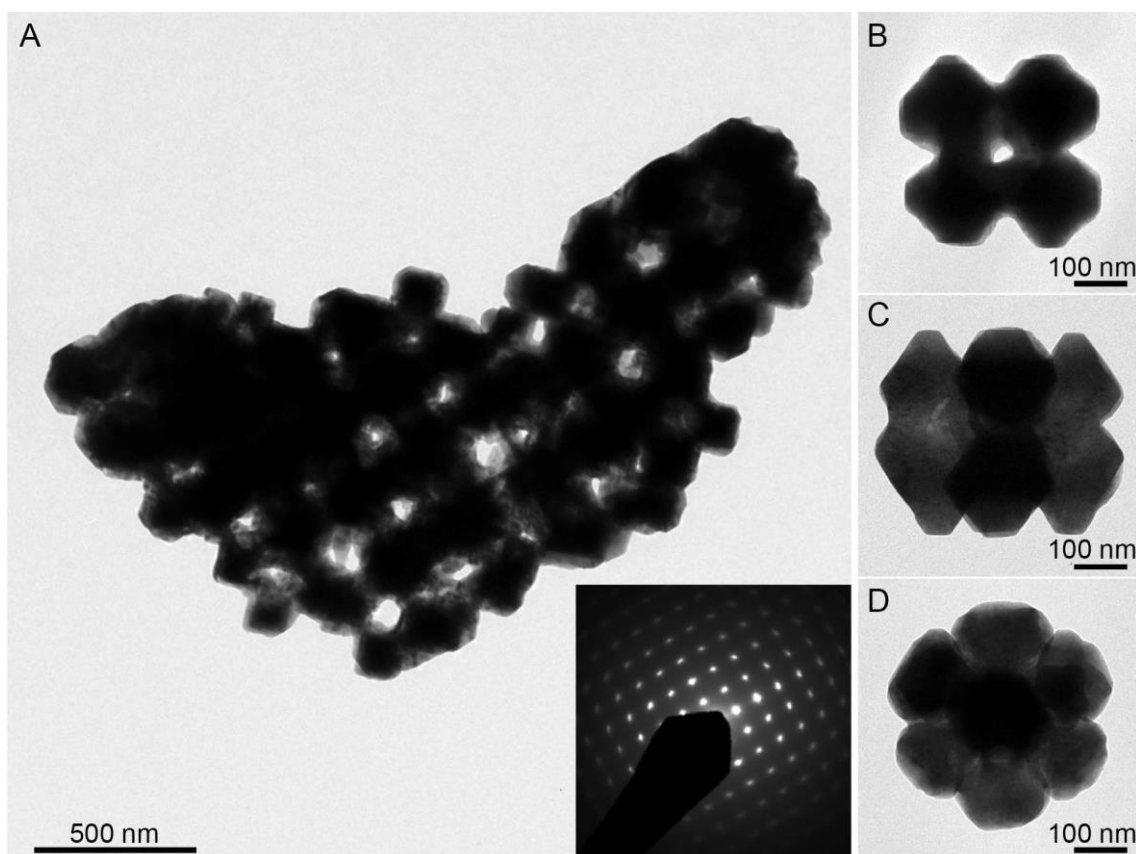


Fig. S7. TEM characterization of Co-Fe PBA CC-2. (A) TEM and SAED images of a typical Co-Fe PBA CC-2. The SAED pattern reveals single crystal feature. (B-D) TEM images of the secondary building blocks for the Co-Fe PBA CC-2 viewed along different directions, further proving that they possess high similarity to the **SOD** clathrate.

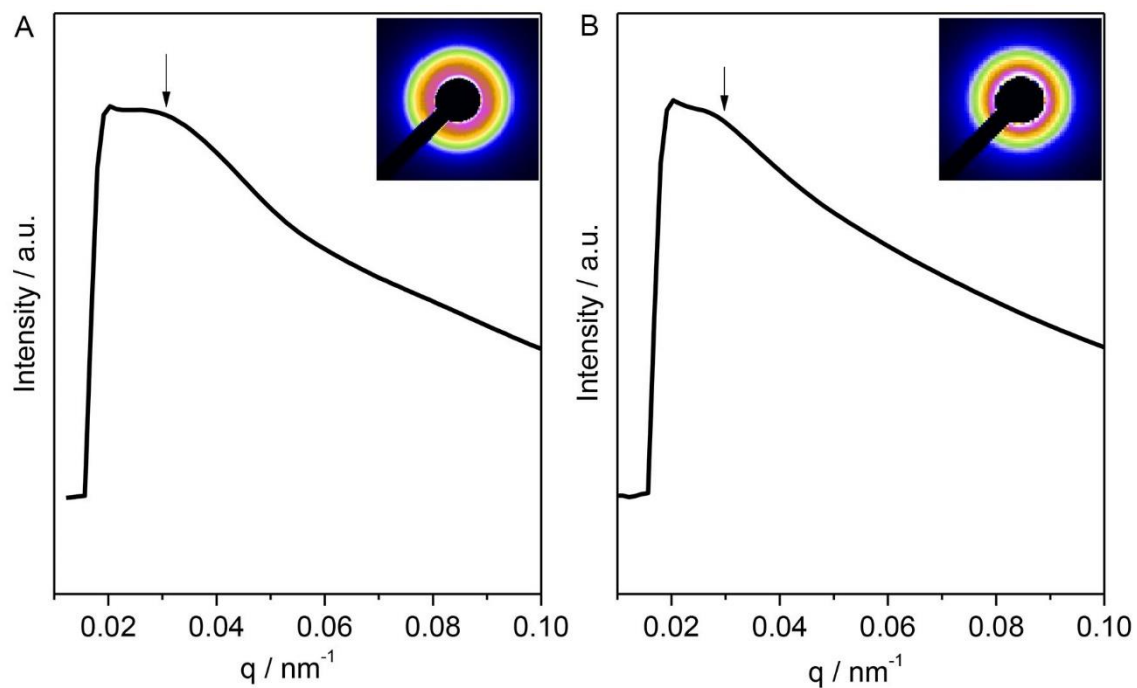


Fig. S8. SAXS data of the samples. (A) Co-Fe PBA CC-1 and (B) Co-Fe PBA CC-2. The arrows show the position of the detected peak, which correspond to 204.5 nm and 212.8 nm for the minimum distance of the orderliness for the CC-1 and CC-2 sample, respectively. These values are close to those estimated from their FESEM images (fig. S3 and S5).

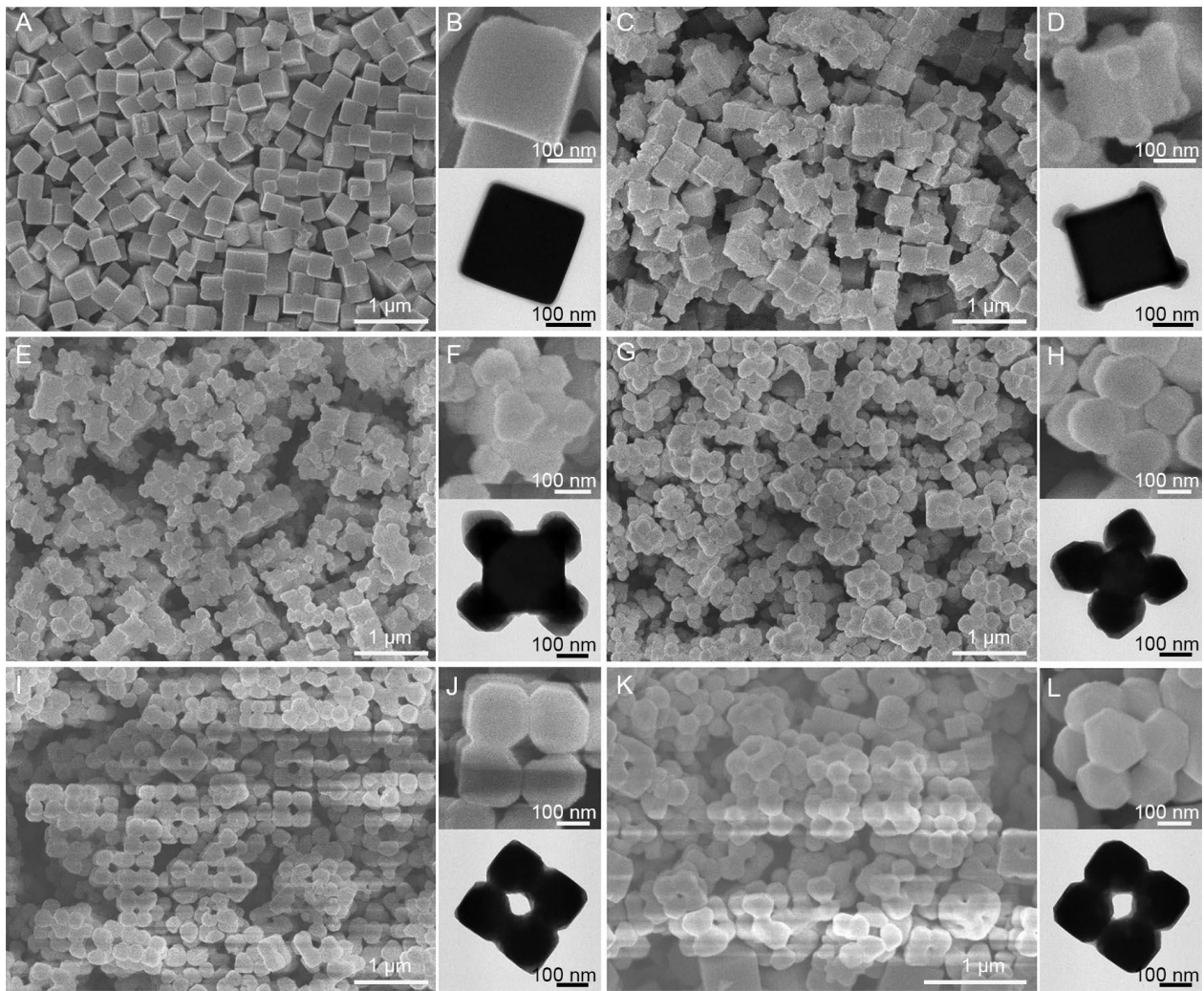


Fig. S9. FESEM and TEM images of the intermediate products for the synthesis of Co-Fe PBA CC-1. The intermediate products are obtained at (A, B) 15 min, (C, D) 30 min, (E, F) 45 min, (G, H) 1 h, (I, J) 2 h and (K, L) 3 h.

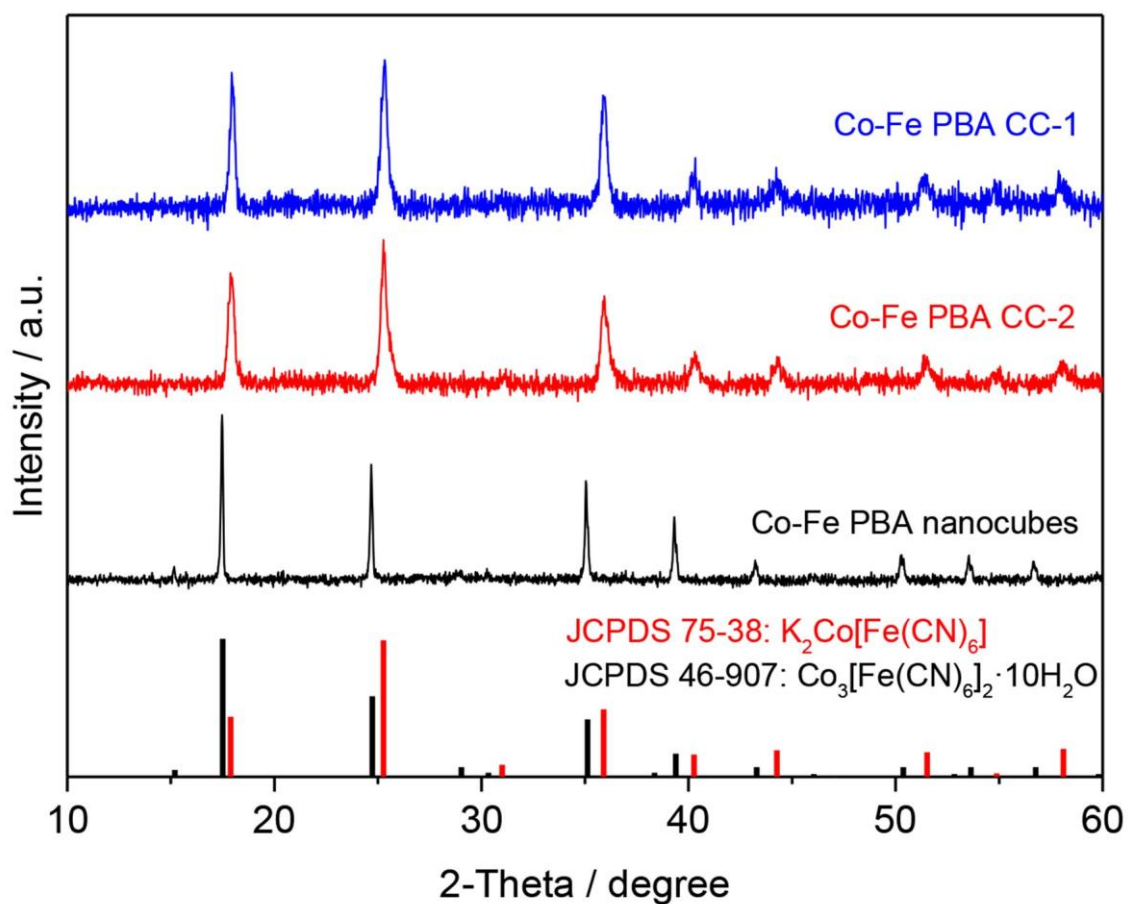


Fig. S10. XRD patterns of different products. The results show a phase transformation occurs in the formation process of both Co-Fe PBA CC-1 and CC-2, that is from the $Co_3[Fe(CN)_6]_2 \cdot 10H_2O$ (denoted as Co_3Fe_2) phase nanocubes to the $K_2Co[Fe(CN)_6]$ (denoted as K_2CoFe) phase CC-1 or CC-2.

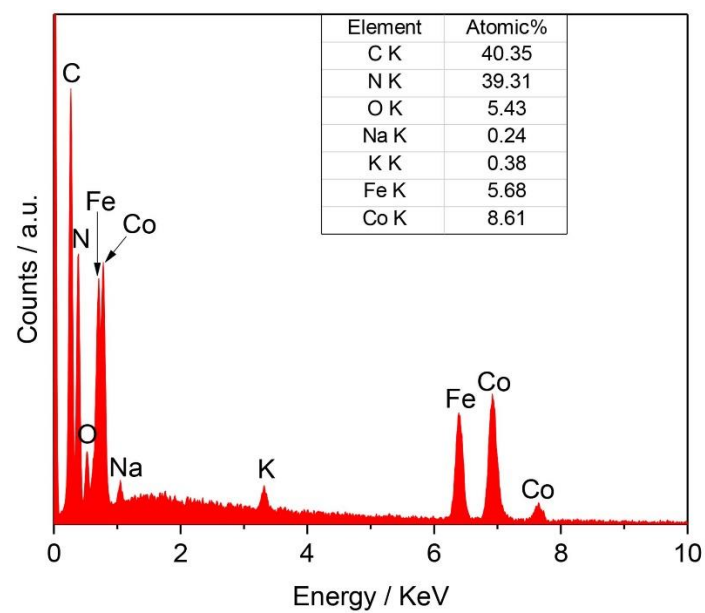


Fig. S11. EDX spectrum of the nanocubes. The data reveal that the product is also a Co-Fe PBA material but with a negligible amount of Na and K. Atomic ratio of Na/K/Fe/Co is 0.03:0.04:0.66:1.

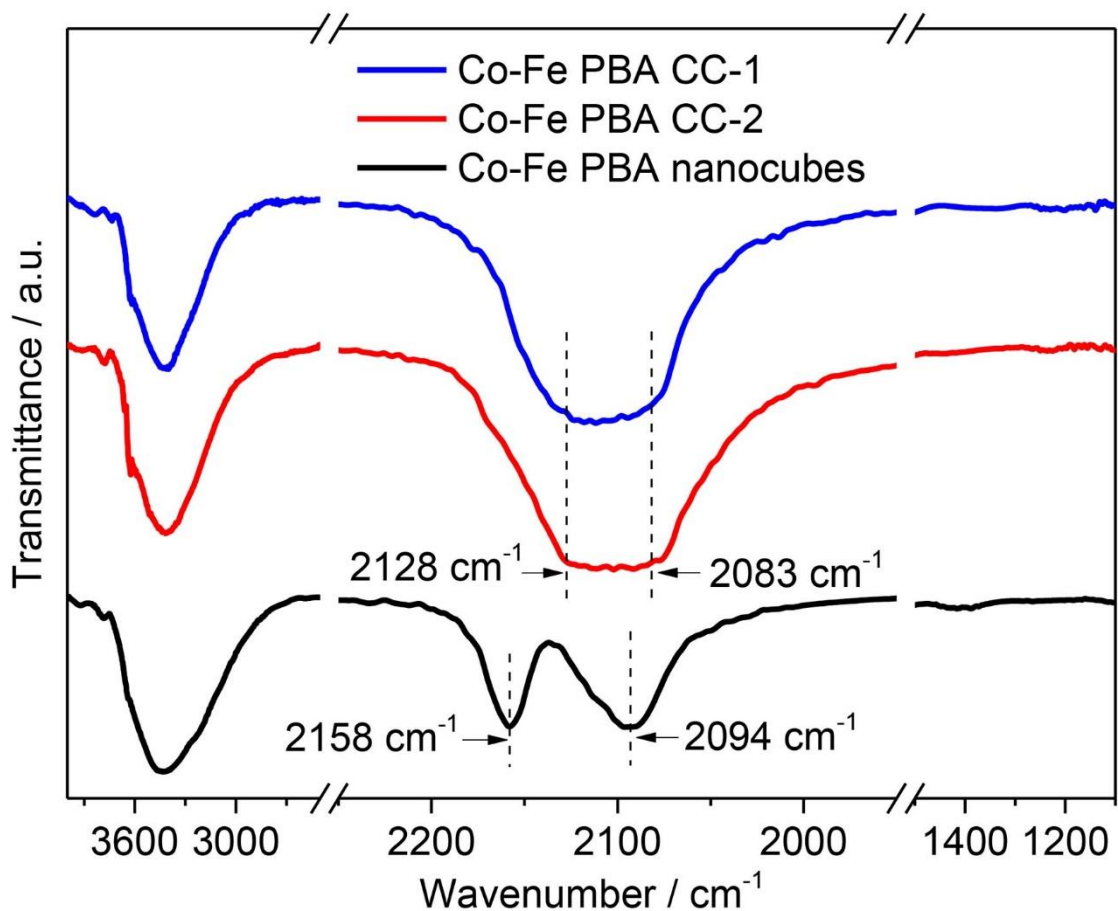


Fig. S12. FTIR spectra of different samples. The peaks assignments of the cyano-group (around 2100 cm⁻¹) can be found in table S2. At the regions of 2800-3000 cm⁻¹ and 1300-1500 cm⁻¹, no obvious peaks can be observed, indicating the absence of the alkane chains on these samples. The broad peak at the region of 2900-3700 cm⁻¹ of each sample could generally be assigned to the vibration of H₂O molecule and hydroxyl group.

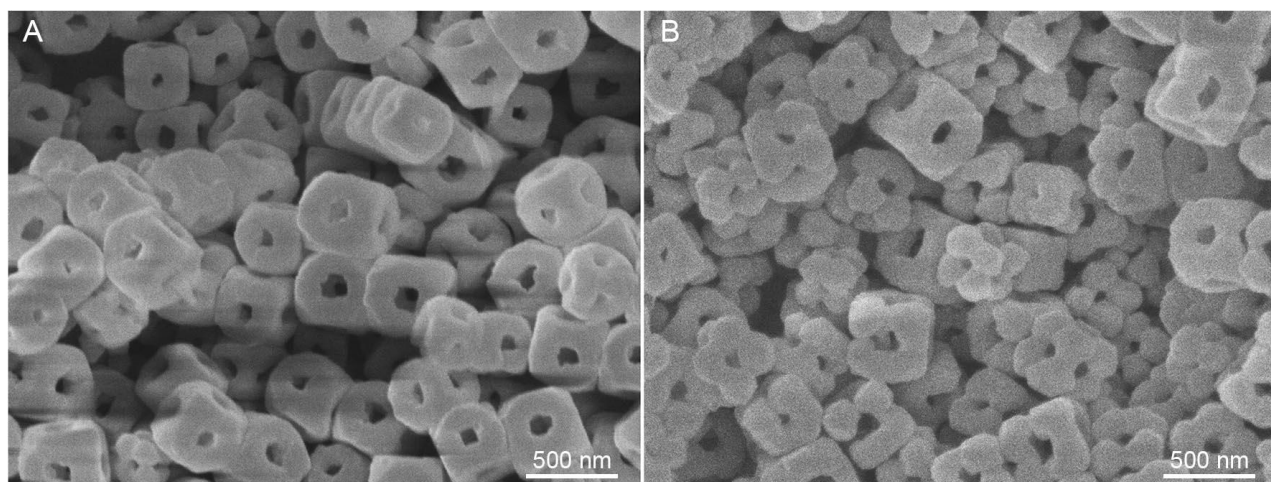


Fig. S13. FESEM images of the control samples with different amounts of SDS. The samples are obtained from the reaction systems with (A) 0 g and (B) 0.5 g of the SDS.

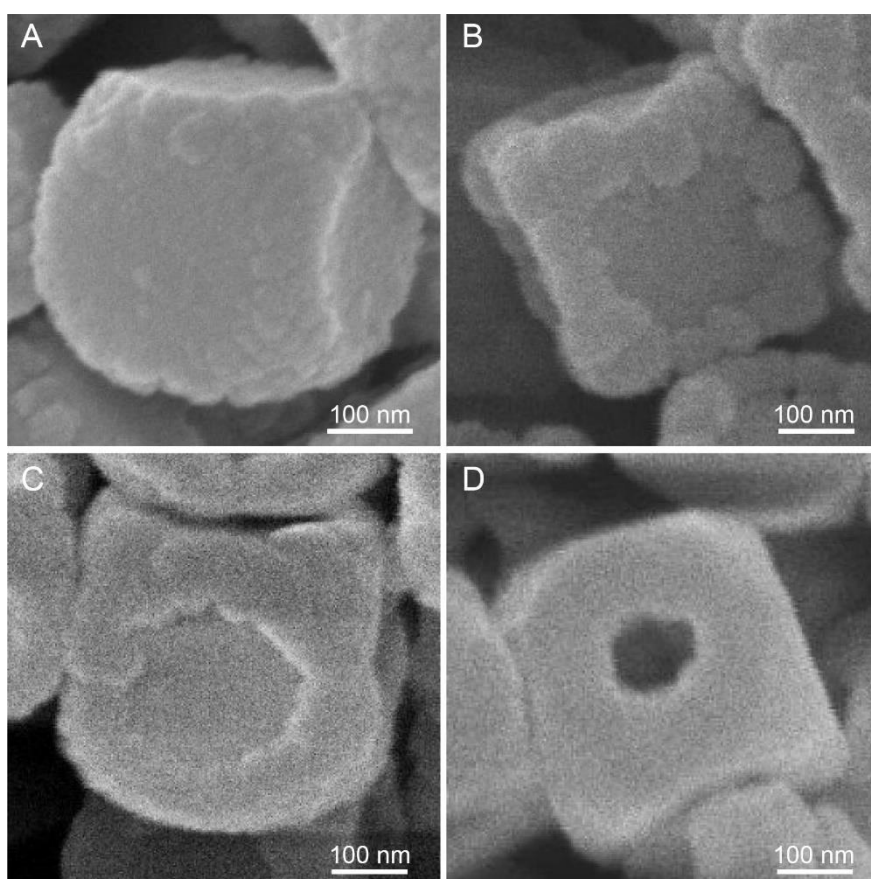


Fig. S14. FESEM images of the intermediate products for the synthesis of the sample with the absence of SDS (as seen in fig. S13A). The products are obtained at (A) 15 min, (B) 30 min, (C) 45 min and (D) 3h.

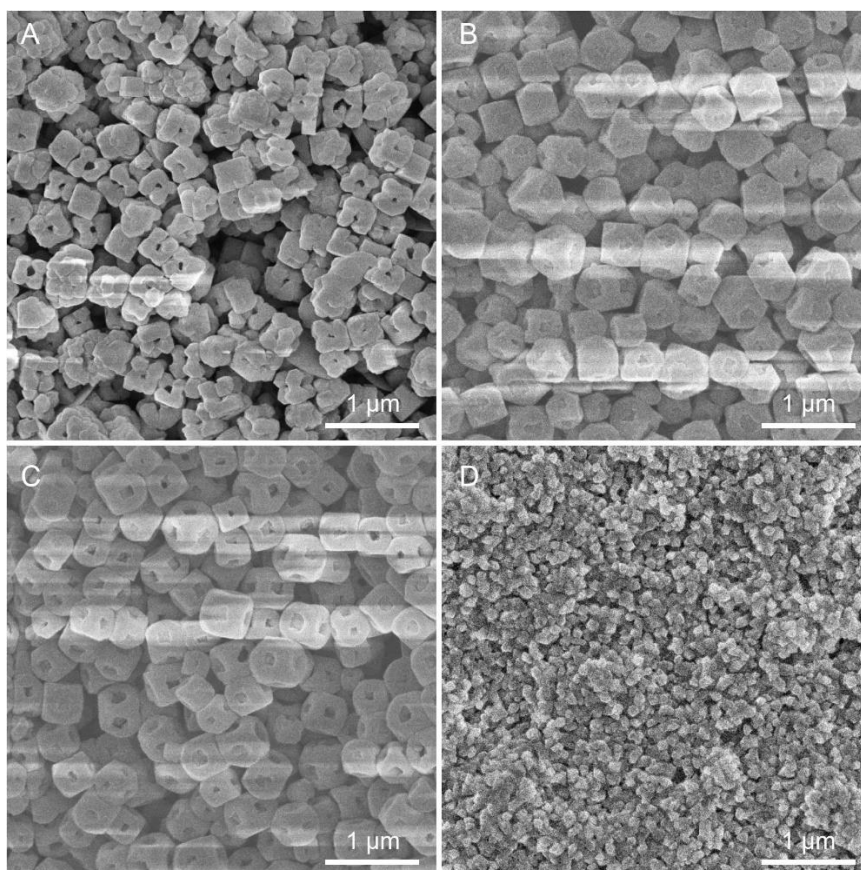


Fig. S15. FESEM images of the control samples with different surfactants. The samples are obtained from the reaction systems with the following surfactants instead of SDS: **(A)** 0.5 g of sodium dodecylbenzenesulfonate (SDBS), **(B)** 1.0 g of polyvinylpyrrolidone (PVP), **(C)** 1.0 g of Pluronic F127 and **(D)** 0.25 g of CTAB.

Discussion: These images show that the reaction with SDBS (anionic surfactant) could possibly produce CCs, but the reactions with PVP, F127 (both are non-ionic surfactants), or CTAB (cationic surfactant) could not. These data mean that the special facts (for example on the edges) of the cores and the SNCs might be charge-sensitive toward the incoming ions, which could accept the site-selected adsorption of the anionic ions but not for the non-ionic ones. This phenomenon is similar with the observations from previous literature that the citrate ions (anionic ion as well) could cap on the side faces of the PBA materials (*Sci. Adv.* **3**, e1700732 (2017)). When using the CTAB, this surfactant and the Co^{2+} ions might have a competitive interaction with the citrate ions. As a result, the weak complexing effect between the Co^{2+} ions and the citrate ions would induce a fast deposition of the PBA materials, leading to the formation of small irregular nanoparticles (*Sci. Adv.* **3**, e1700732 (2017)).

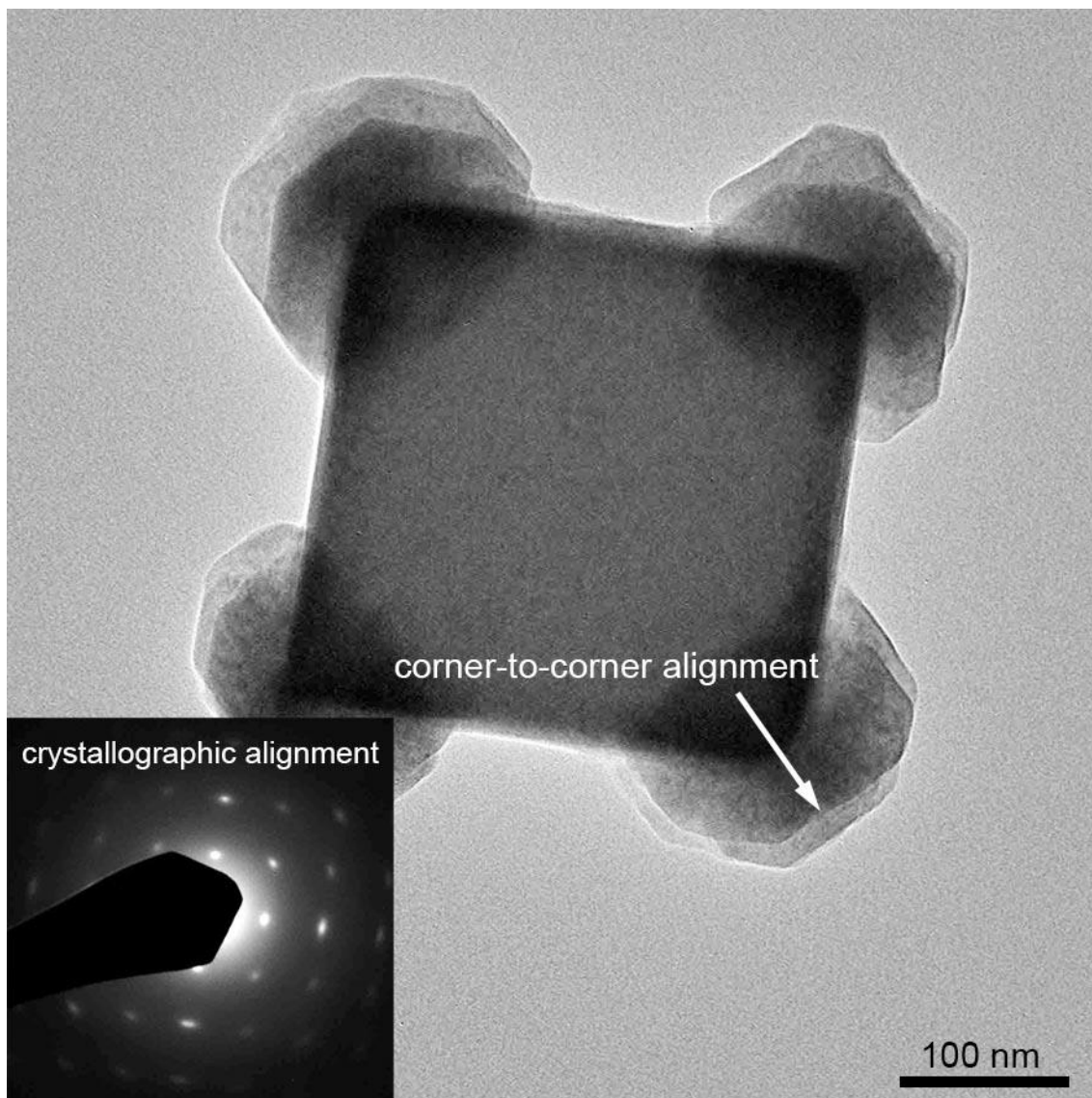


Fig. S16. TEM and SAED images of a typical core@satellite superstructure obtained at the reaction time of 45 min for the synthesis of Co-Fe PBA CC-1. The SAED patterns of the core and satellites here should be overlap and hardly distinguished from each other due to their close unit cell parameters, as revealed by the XRD data in fig. S9. The morphological and crystallographic alignments indicate the epitaxial growth of SNCs on the core.

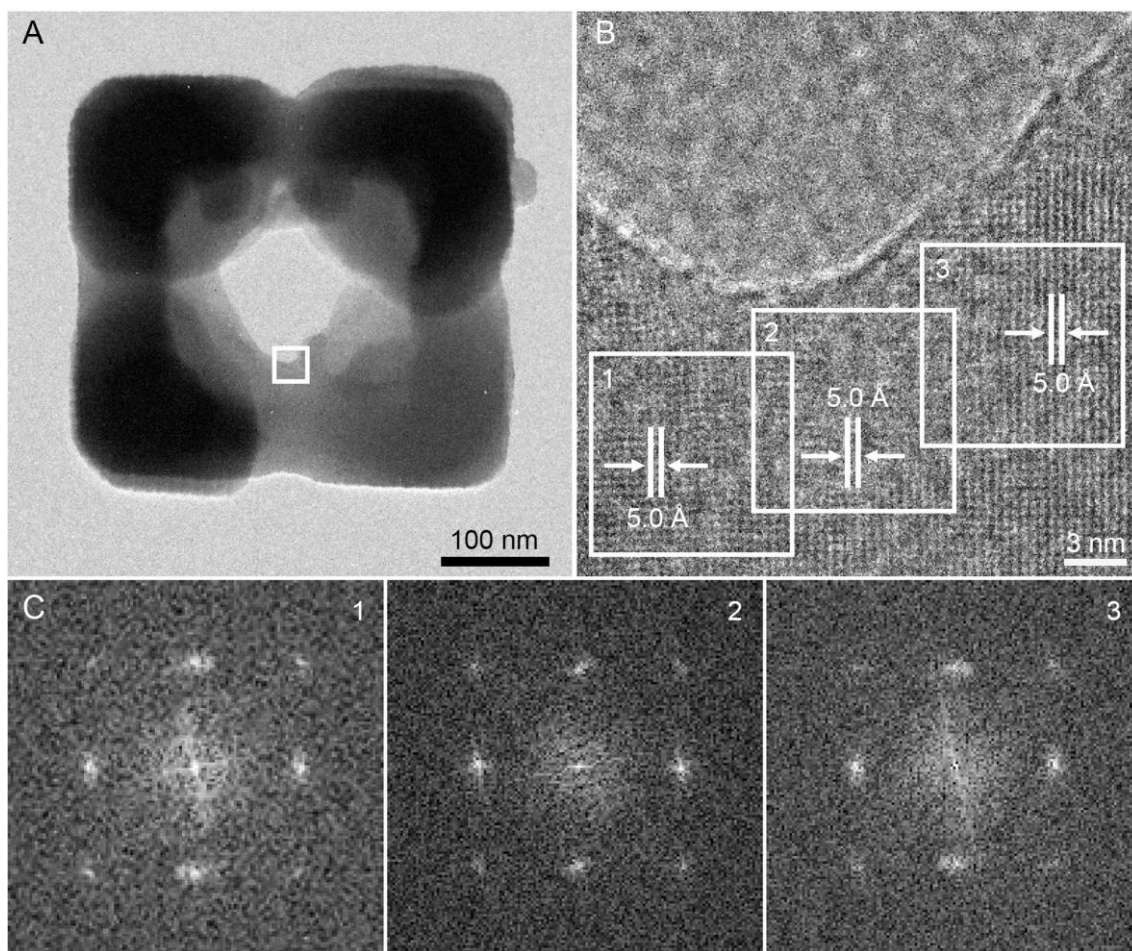


Fig. S17. Characterization of a typical Co-Fe PBA CC-1 particle. (A) TEM image. (B) HRTEM image obtained from the marked area in (A), displaying continuous lattice fringes across the attachment region of the adjacent NCs. The interplanar spacing of 5.0 Å should be indexed to the {200} planes. (C) FFT images derived from the marked area in (B) show identical patterns.

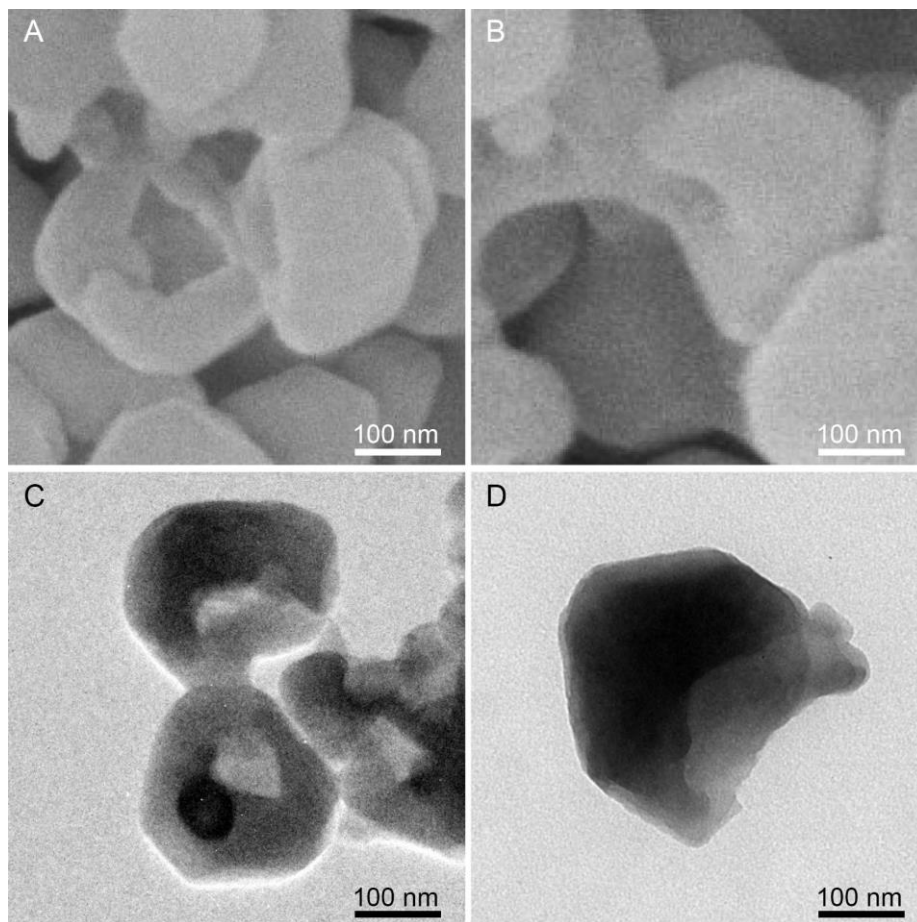


Fig. S18. Characterization of some isolated SNCs that fall off the core at the reaction time of 1 hour for the synthesis of Co-Fe PBA CC-1. (A, B) FESEM and (C, D) TEM images.

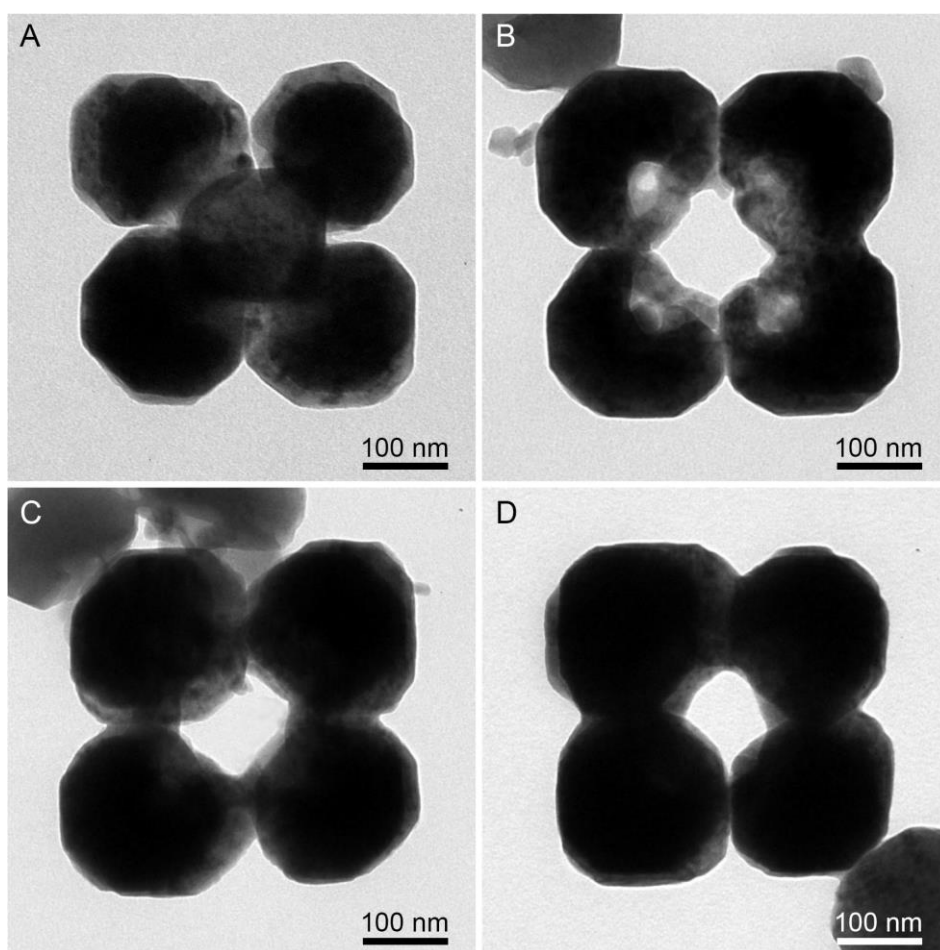


Fig. S19. TEM images of the typical particle obtained at different reaction times for the synthesis of Co-Fe PBA CC-1. (A) 1, (B) 1.25, (C) 1.5 and (D) 2 h. These images show the evolution process of the building blocks from incomplete to complete solid NCs.

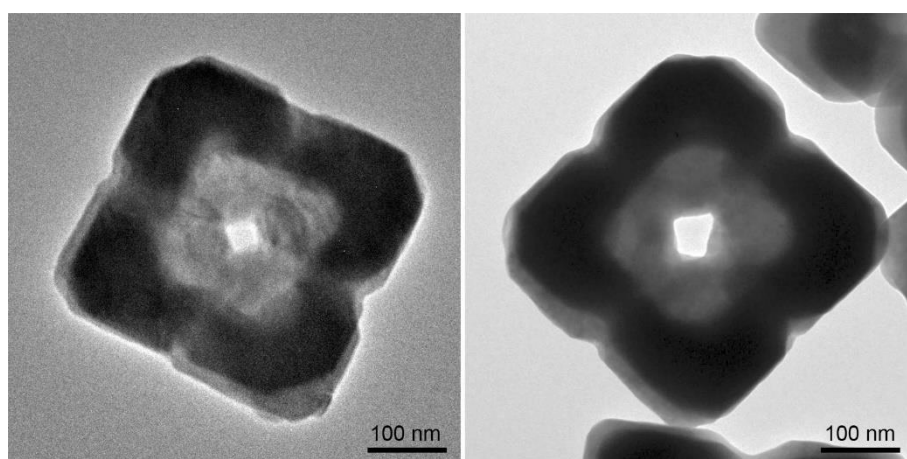


Fig. S20. TEM images of some occasionally observed particles in the sample of Co-Fe PBA CC-1. These images show special CCs where the building blocks are 3/4 solid and 1/4 hollow.

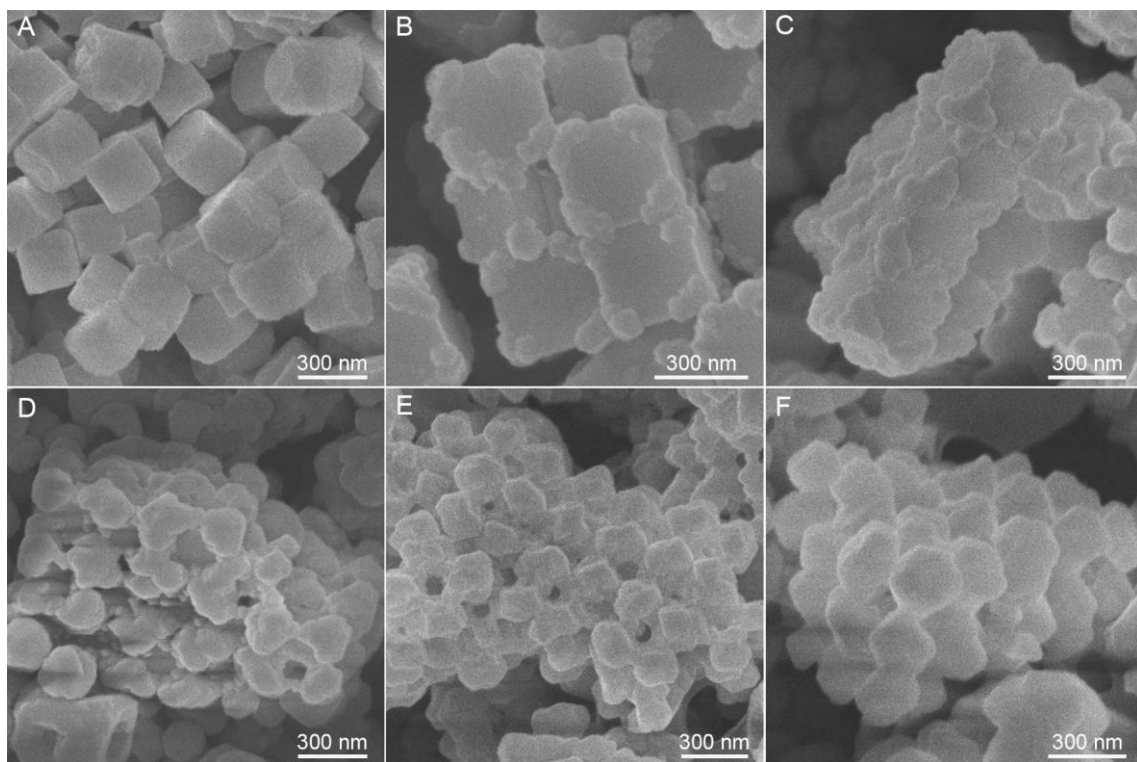


Fig. S21. FESEM images of the intermediate products for the synthesis of Co-Fe PBA CC-2.

The products are obtained at (A) 15 min, (B) 30 min, (C) 45 min, (D) 1 h, (E) 2 h and (F) 3 h.

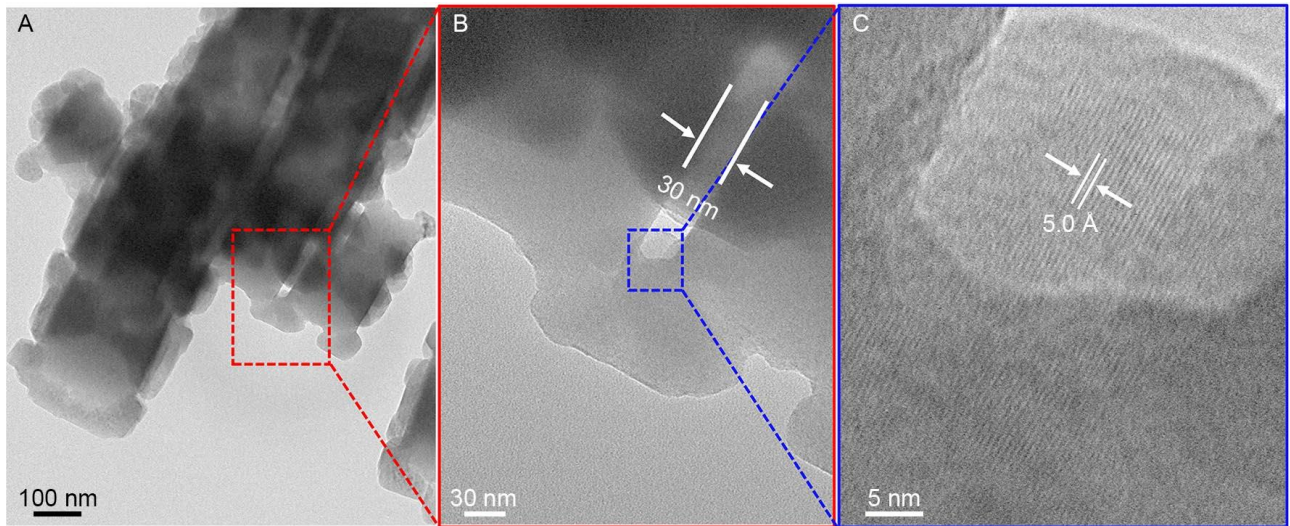


Fig. S22. Characterization of the core@satellite superstructures obtained at the reaction time of 45 min for the synthesis of Co-Fe PBA CC-2. (A) TEM image. (B) TEM image shows a gap between adjacent core particles with a width of 30 nm. (C) HRTEM image displays continuous lattice fringes across the attachment region of the attached SNCs. The interplanar spacing of 5.0 Å should be indexed to the {200} planes. All these data indicate an OA process takes place between the SNCs along the $\langle 100 \rangle$ directions.

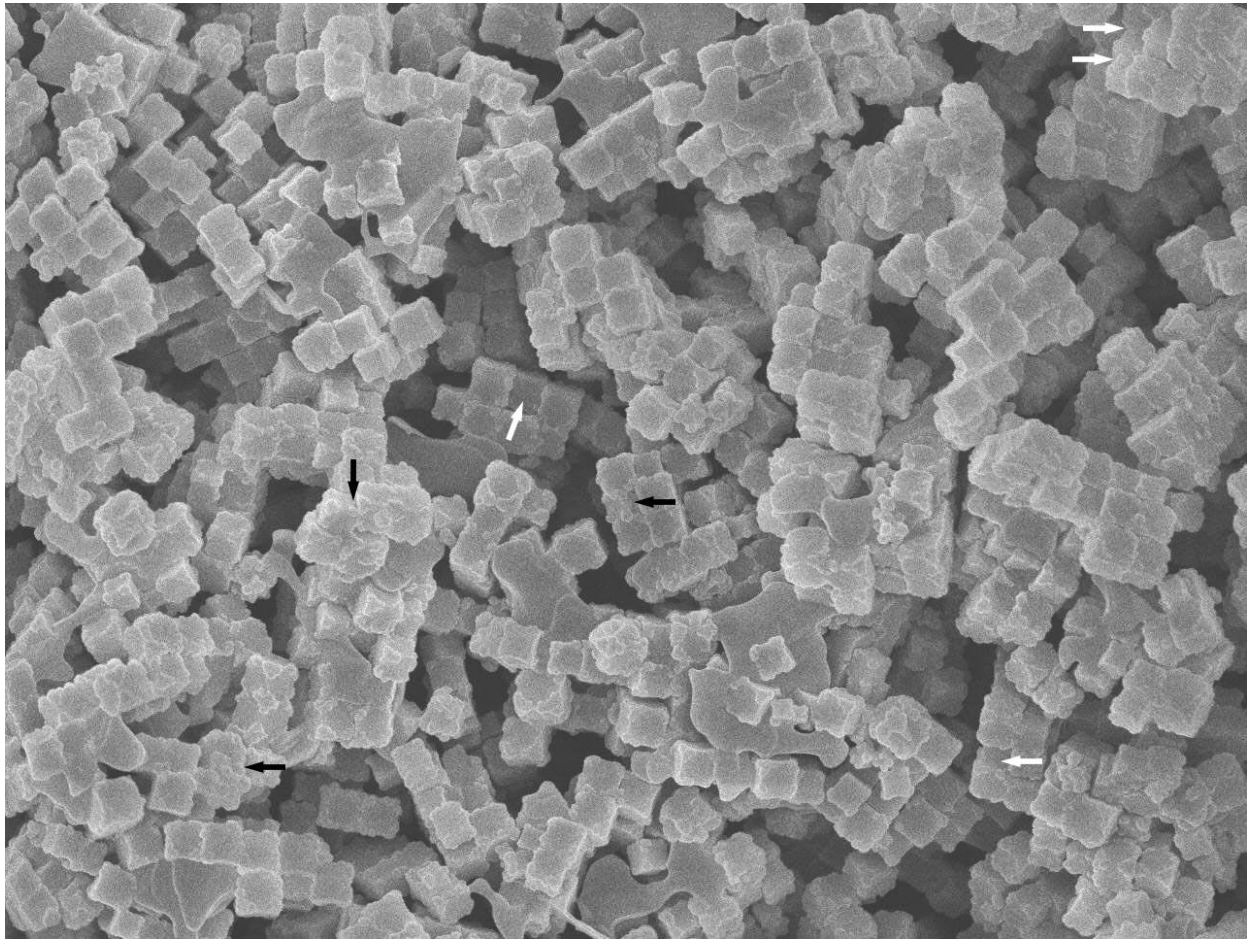


Fig. S23. A FESEM image shows the assembly imperfections in the packing of the **core@satellite superstructures**. White arrows point out the spatial misalignments while the black arrows point out the rotations among adjacent particles.

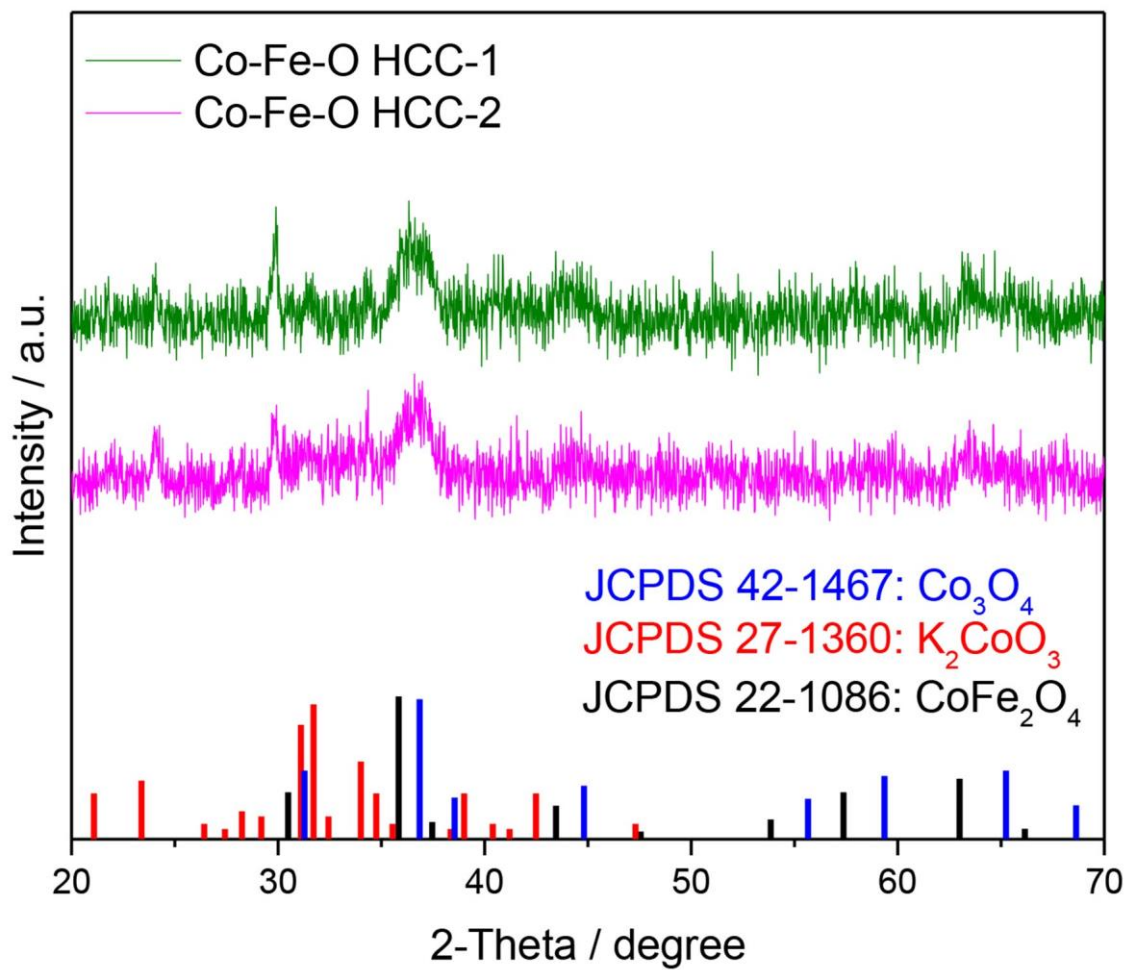


Fig. S24. XRD patterns of the Co-Fe-O HCCs that derived from the Co-Fe PBA CCs. XRD results reveal that both of the samples are Co-Fe oxide composites composed of Co_3O_4 , CoFe_2O_4 and K_2CoO_3 .

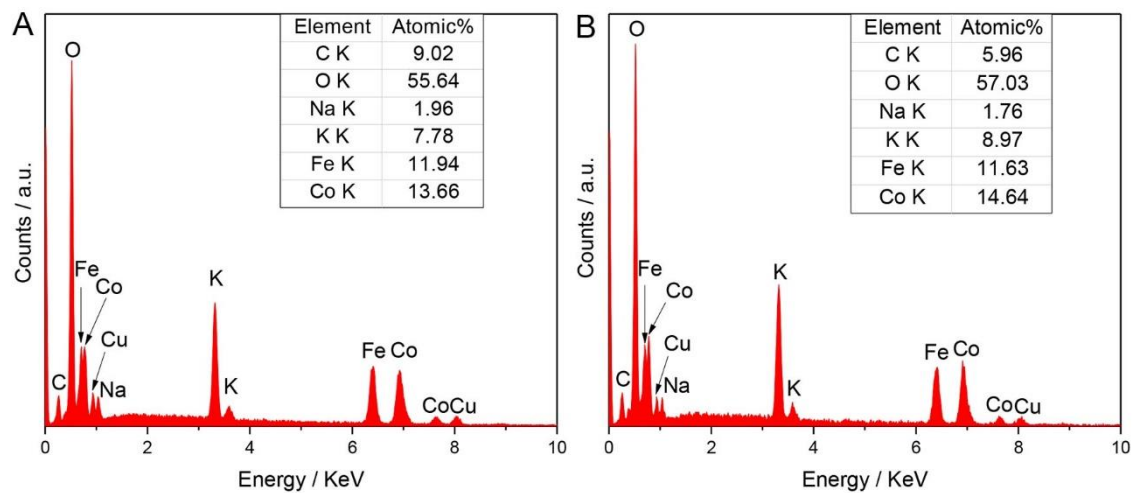


Fig. S25. EDX spectra of the Co-Fe-O HCCs derived from the Co-Fe PBA CCs. (A) HCC-1 and (B) HCC-2. The Cu signal should come from the substrate.

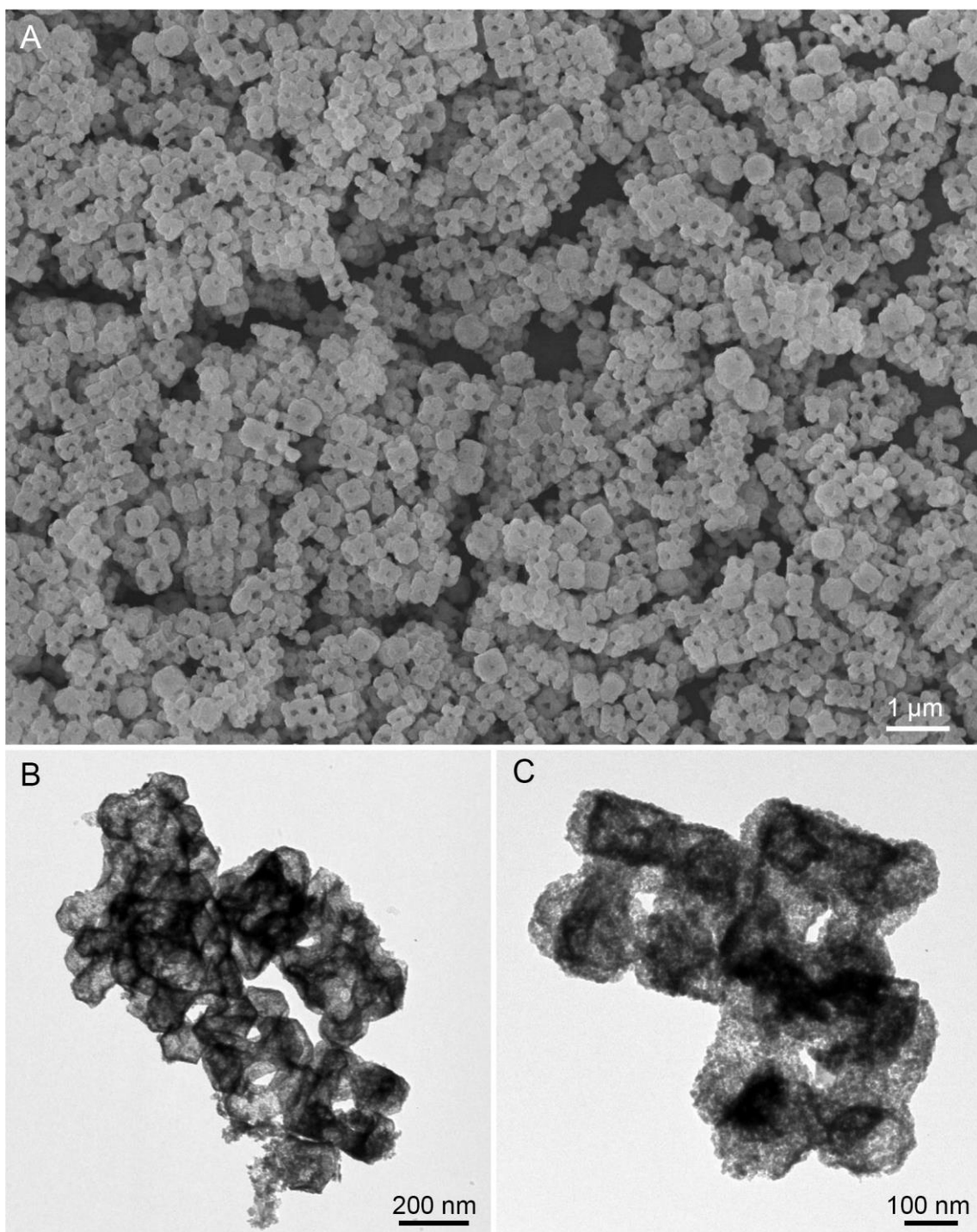


Fig. S26. Characterization of Co-Fe-O HCC-1. (A) FESEM and (B, C) TEM images.

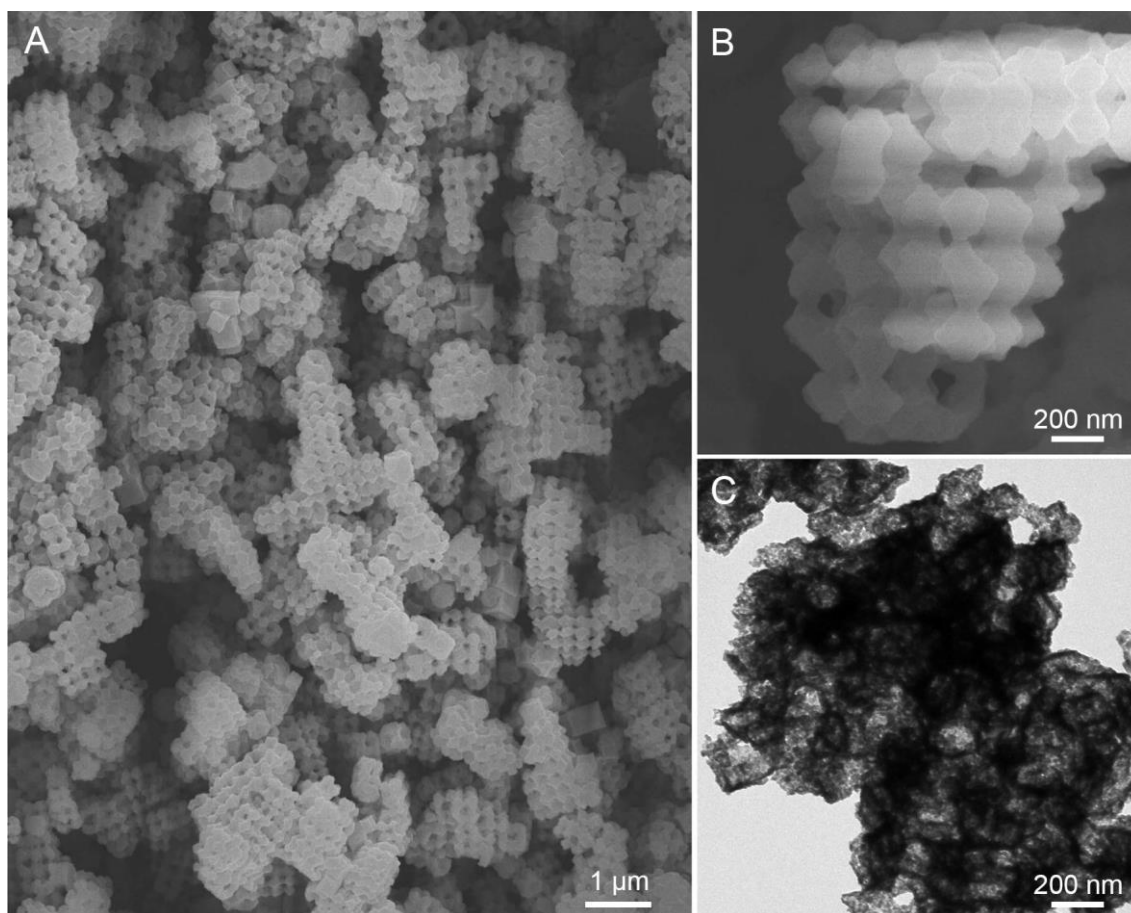


Fig. S27. Characterization of Co-Fe-O HCC-2. (A, B) FESEM and (C) TEM images.

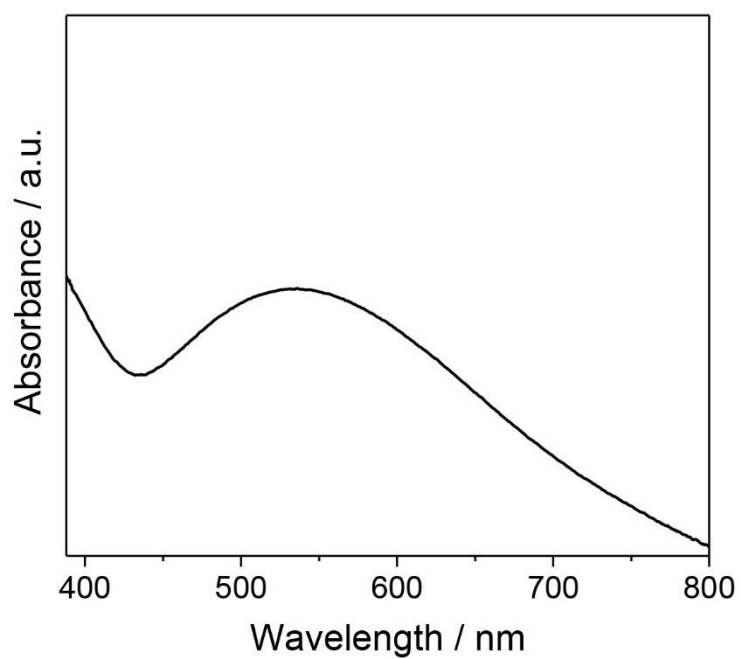


Fig. S28. Light absorption spectrum of the Co-Fe PBA CC-1 catalyst.

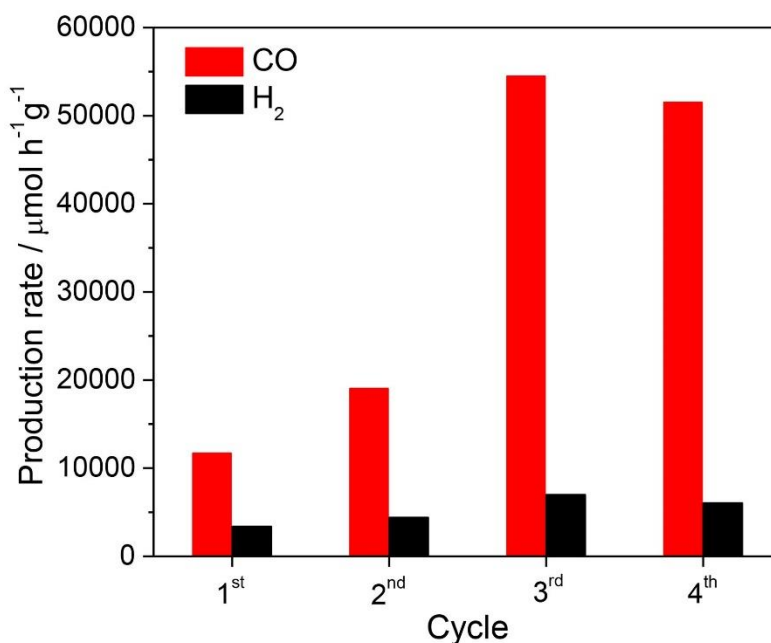


Fig. S29. Stability tests of the Co-Fe PBA CC-1 catalyst for CO₂ photoreduction. The experiments were performed by adding the fresh **Ru** photosensitizer into the system after 1 h reaction (the first cycle) and then re-start the reaction for another three cycles.

Discussion: After adding fresh **Ru**, the system shows high photocatalytic CO₂ reduction activity for the next two runs (the second and the third cycle), indicating the Co-Fe PBA CC-1 catalyst is stable for the reaction. The small activity loss in the fourth cycle is induced by the light shielding effect of excessive **Ru**, consistent with the results of previous works (e.g., *Angew. Chem. Int. Ed.* **53**, 1034 (2014); *Appl. Catal. B Environ.* **224**, 1009 (2018)).

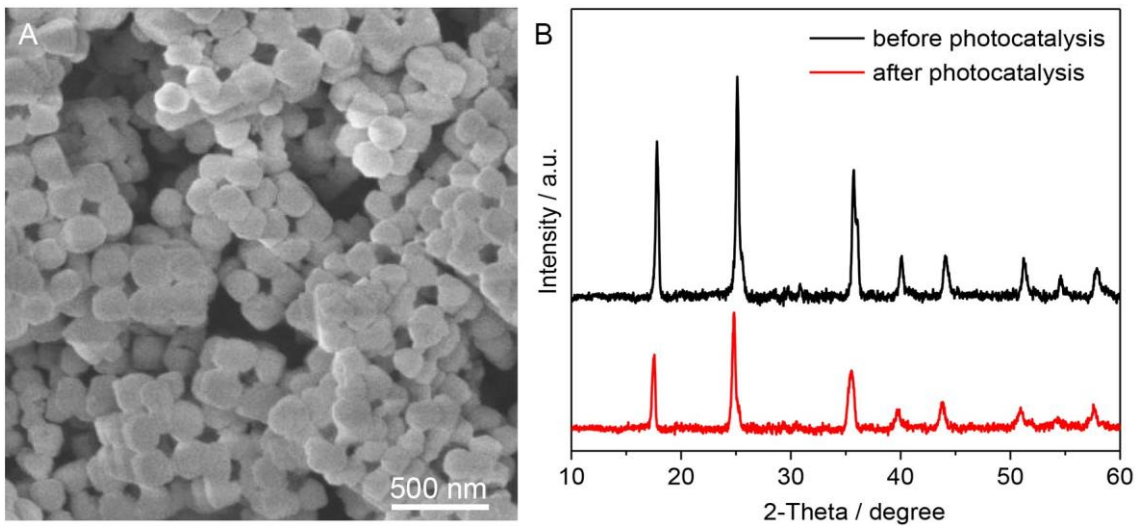


Fig. S30. Characterizations of the Co-Fe PBA CC-1 catalyst after the photocatalysis. (A)

FESEM image of the sample. **(B)** XRD data of the sample.

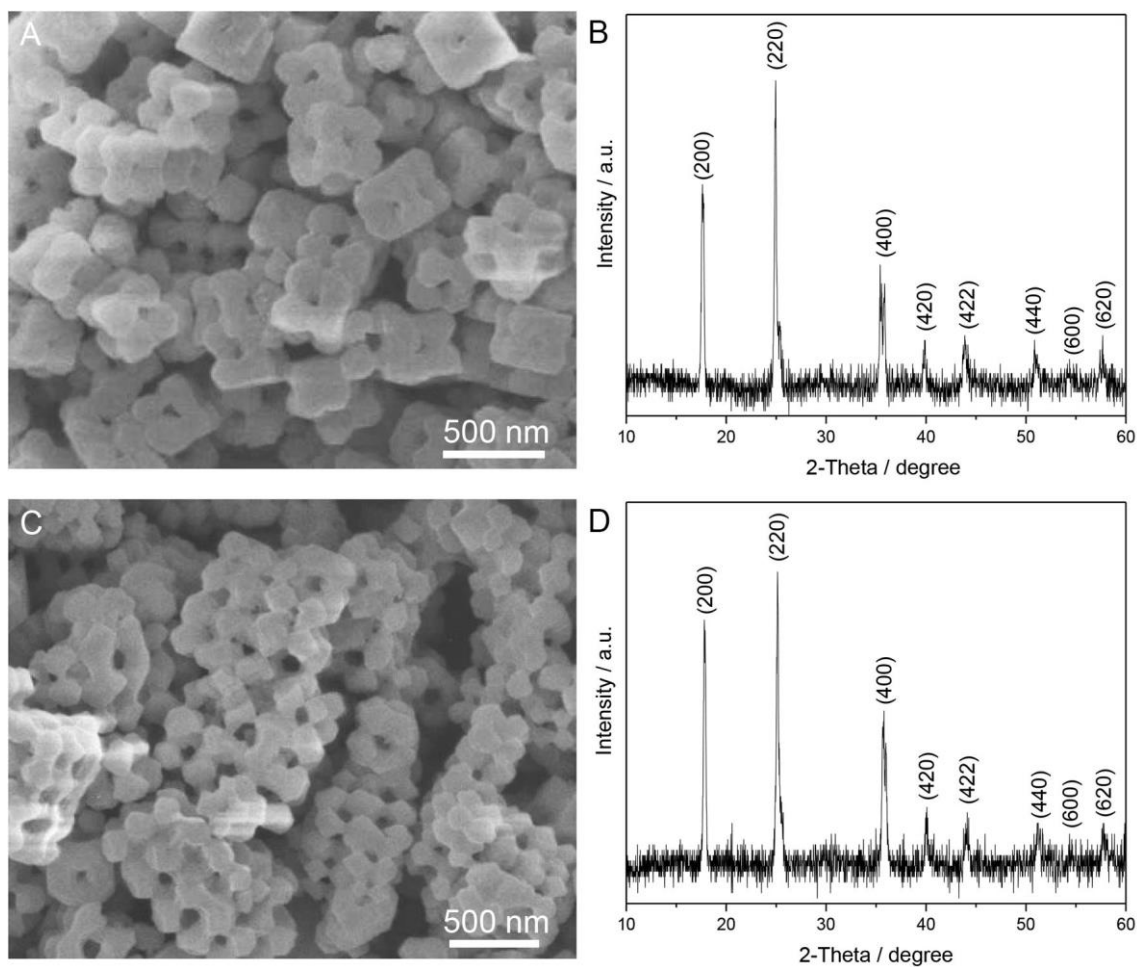


Fig. S31. Characterization of the Co-Fe PBA CCs after storage as powder in air for more than 6 months. (A) FESEM and (B) XRD data of the CC-1 sample. (C) FESEM and (D) SEM data of the CC-2 sample. FESEM images show that the morphology of the CCs, including the shape of the building blocks and their tight connection, retains well as compared with those as-prepared samples (fig. S3 and S5). XRD data exhibit that the samples after long-term storage still possess good crystallinity. These results demonstrate that the CC materials have good stability.

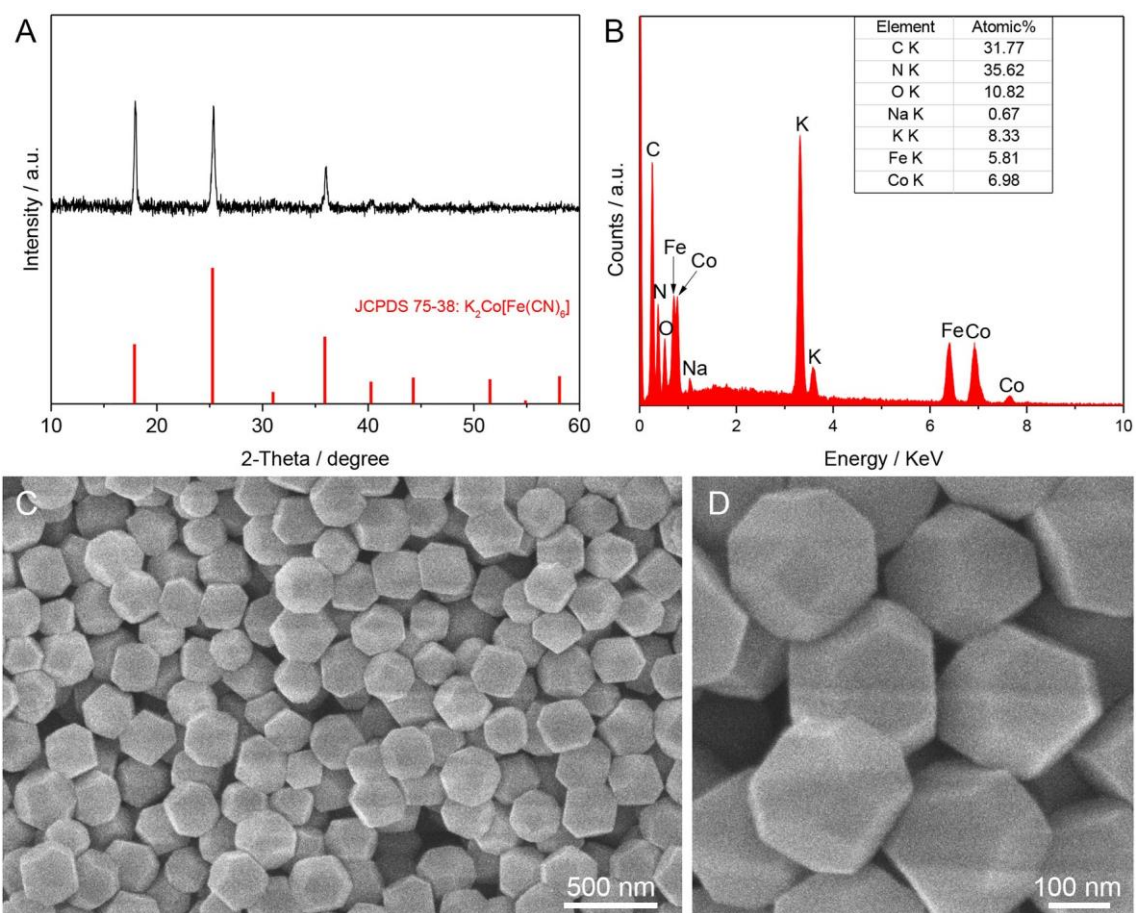


Fig. S32. Characterization of the Co-Fe PBA NPs as a catalyst without colloidal assembly. (A) XRD, (B) EDX and (C, D) SEM images.

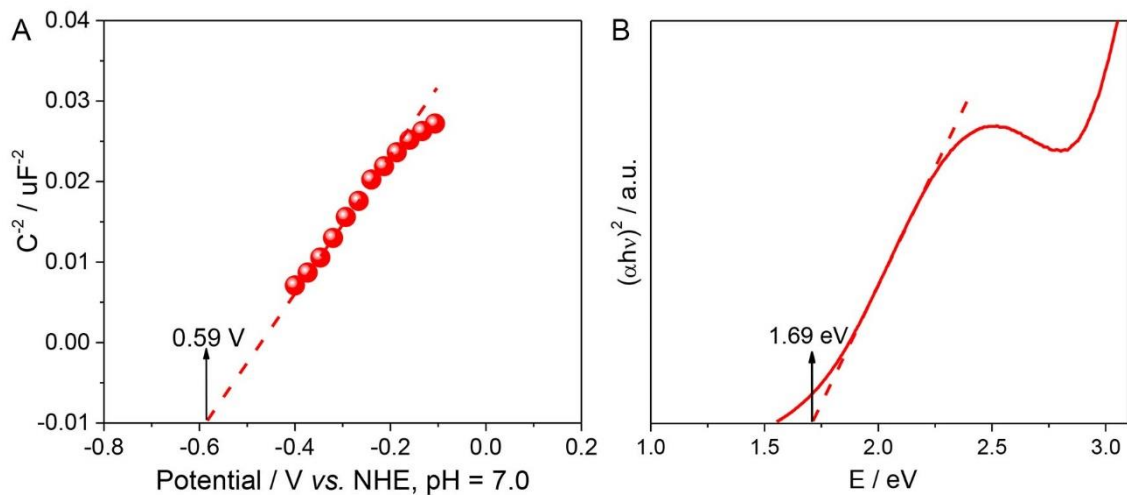


Fig. S33. Electrochemical measurements of the Co-Fe PBA CC-1 catalyst. (A) Mott-Schottky plot and (B) Tauc plot. The derived flat-band potential from the Mott-Schottky plot is -0.59 V (vs. NHE), corresponding to the conduction band potential. The band gap energy of the catalyst is about 1.69 eV estimated from the Tauc plot. Therefore, the valence band potential of the catalyst is about 1.10 V (vs. NHE).

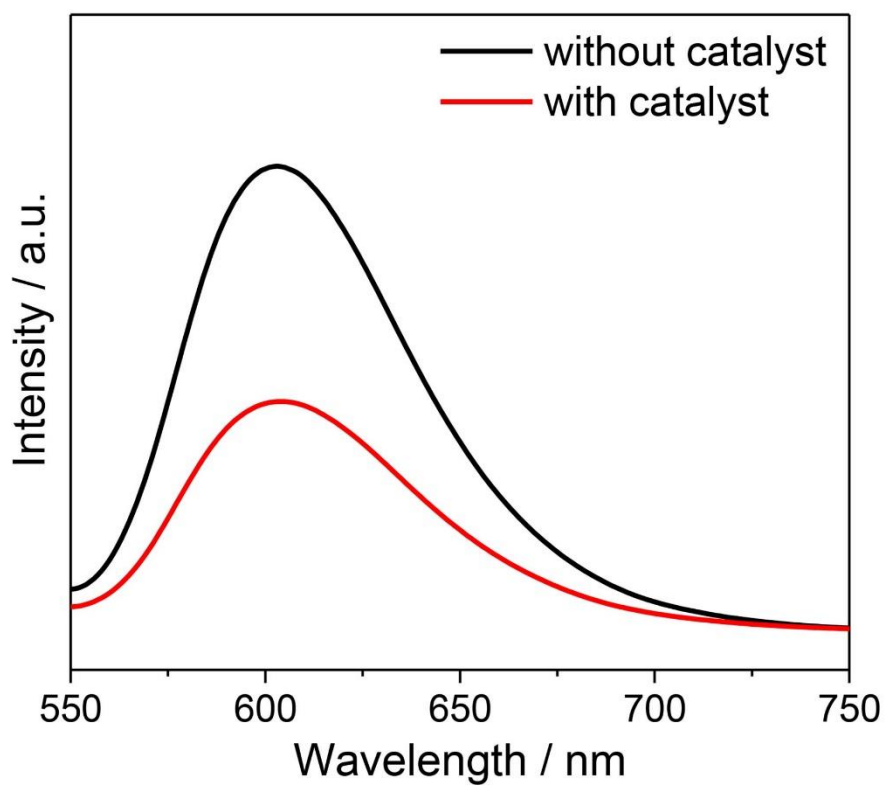


Fig. S34. Room temperature PL spectra of the reaction systems with and without the Co-Fe PBA CC-1 catalyst.

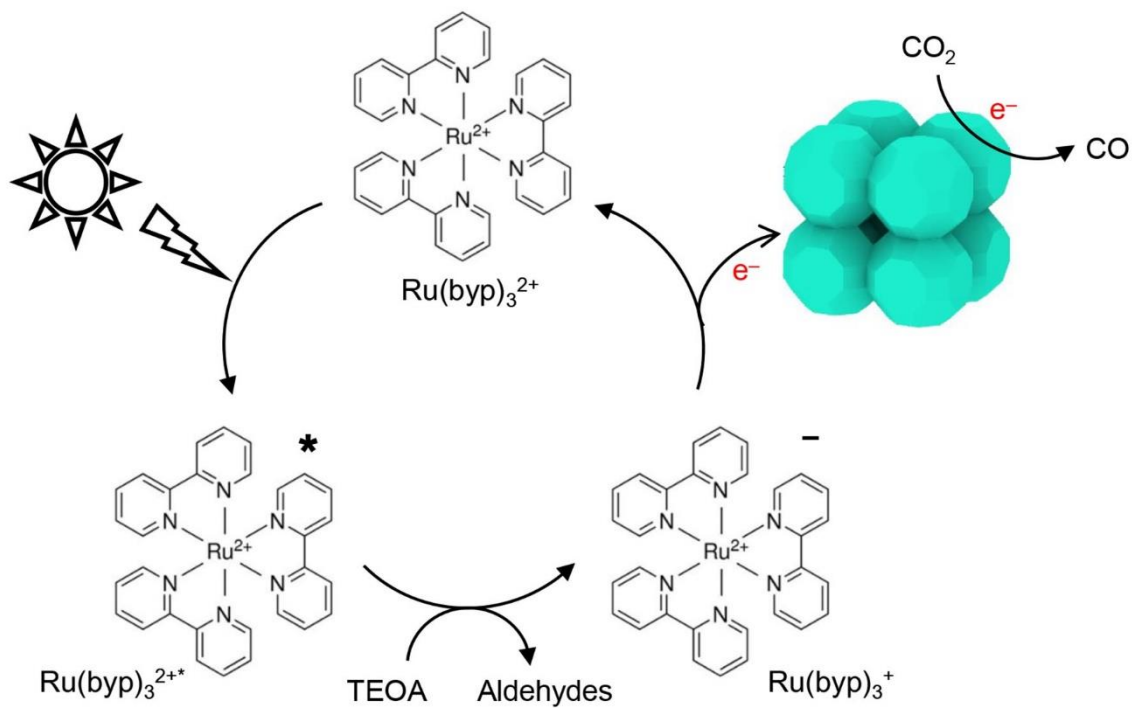


Fig. S35. Proposed mechanism for the photocatalytic conversion of CO₂ to CO.

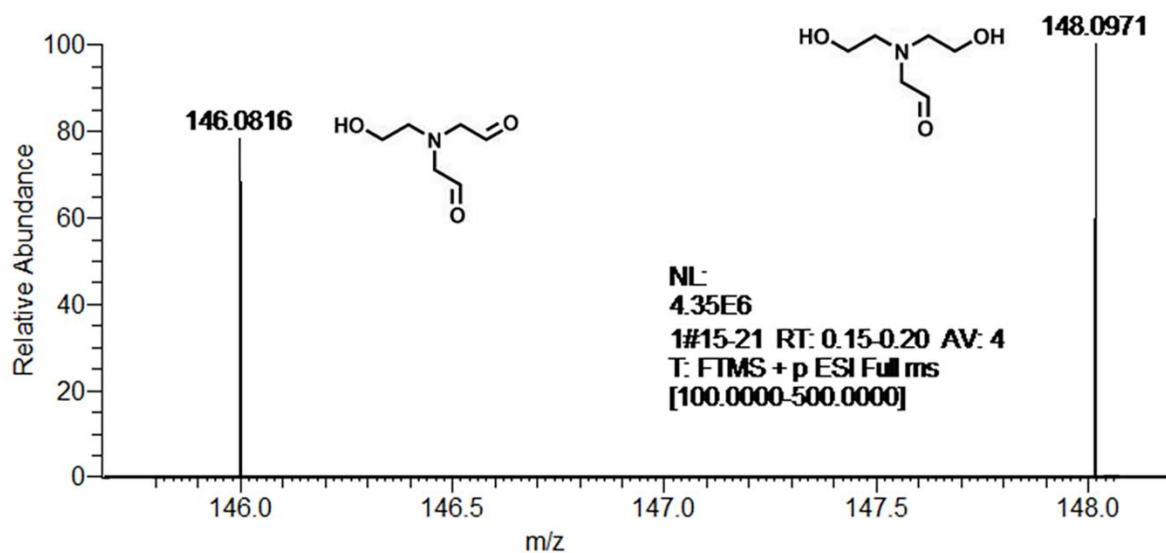


Fig. S36. Liquid chromatography–mass spectrometry analyses of the oxidation species.

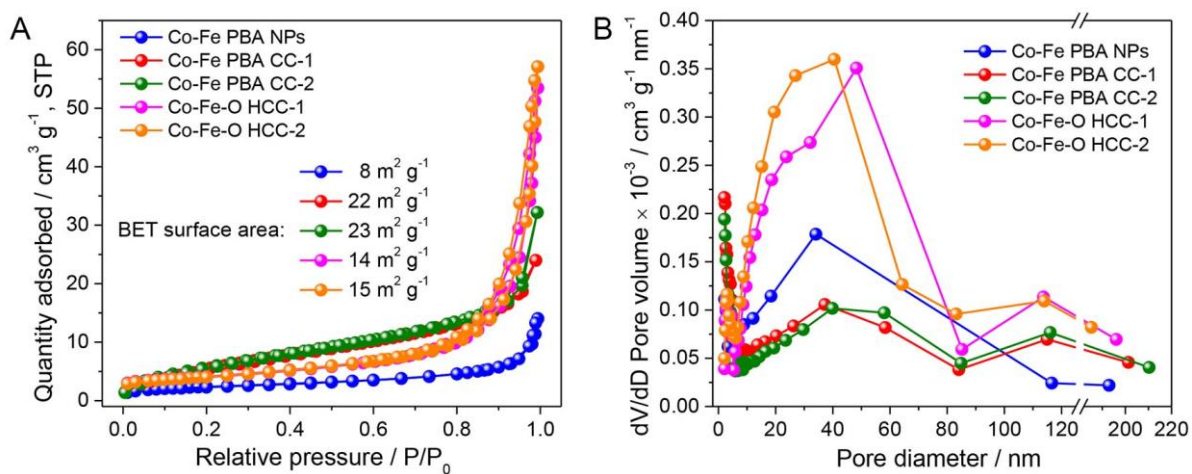


Fig. S37. N₂ adsorption measurements of diverse catalysts. **(A)** Adsorption-desorption isotherms of the samples. **(B)** Pore size distribution of the samples.

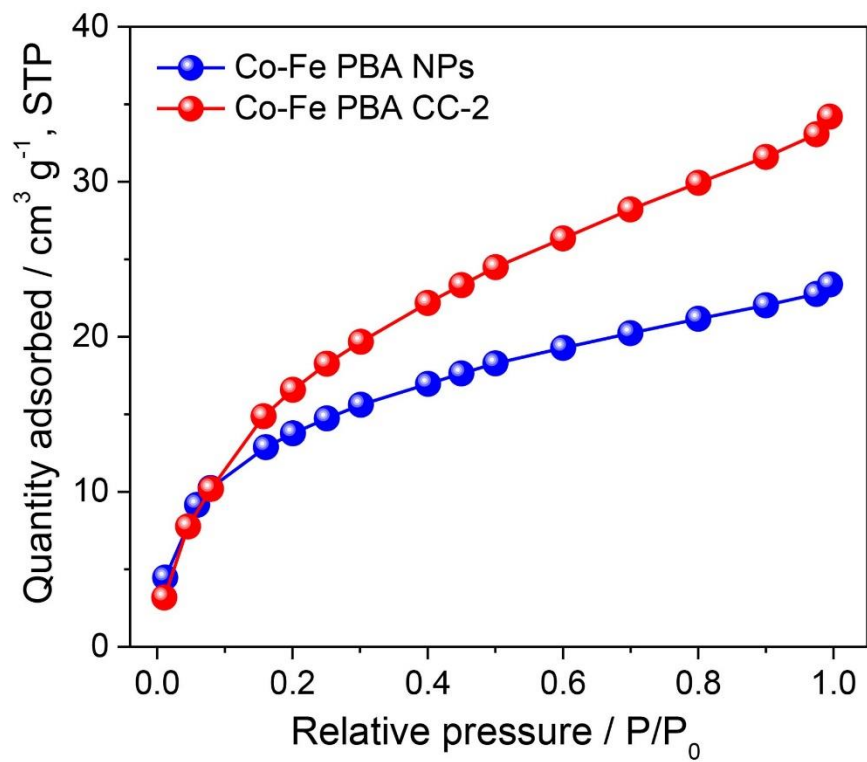


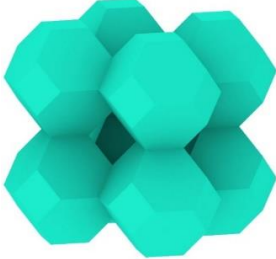


Fig. S38. CO₂ adsorption isotherms of Co-Fe PBA CC-2 and Co-Fe PBA NPs.

Table S1. Some parameters of the Co-Fe PBA CCs.

	CC-1	CC-2
Supercrystal Unit Cell	primitive cubic $a = 204.5 \text{ nm}^*$, $\alpha = 90^\circ$	primitive cubic $a = 212.8 \text{ nm}^*$, $\alpha = 90^\circ$
Point Group	$Pm\bar{3}m$	
Topological Nets	primitive cubic (pcu), octahedral symmetry	
Attached Manner	face-to-face ($\{100\}$ facets)	
Primary Building Block	 t-grc	 t-toc
Secondary Building Block	—	

*The value is obtained from the SAXS data (fig. S8).

Table S2. The position of FTIR peaks of the samples and their assignment.

Samples	$\nu(\text{CN}) \text{ cm}^{-1}$ $\text{Co}^{\text{II}}\text{-N}\equiv\text{C-Fe}^{\text{III}}$	$\nu(\text{CN}) \text{ cm}^{-1}$ $\text{Co}^{\text{II}}\text{-N}\equiv\text{C-Fe}^{\text{II}}$	$\nu(\text{CN}) \text{ cm}^{-1}$ $\text{Co}^{\text{III}}\text{-N}\equiv\text{C-Fe}^{\text{II}}$
nanocubes	2158	2094	—
CC-1/CC-2	—	2083	2128

Table S3. Similarities of the entropic and enthalpic valence of NCs and their operations in the assembly.










Category	{100}	{110}	{111}
Crystal shapes (entropic)			
	cube	granatohedron	octahedron
Crystal planes (enthalpic)			
Operations	{100}	{110}	{111}
Assembling geometry			
	<i>octahedron</i>	<i>cuboctahedron</i>	<i>cube</i>
Angles for incoming building blocks	90°, 180°	60°, 90°, 120°, 180°	70.5°, 105.5°, 180°
Maximum bonds	6	12	8

Table S4. Comparison of the photocatalytic CO₂ reduction performance of the Co-Fe PBA CCs prepared in this work with some recently reported advanced catalysts.

Catalysts	Photosensitizer/ sacrificial agent	Major product evolution rate ($\mu\text{mol h}^{-1} \text{g}^{-1}$)	Ref.
Co-Fe PBA CC-1		CO: 11700	this work
Co-Fe PBA CC-2		CO: 14200	
Zr-bpdc/RuCO		CO: 2328 HCCOH: 7991	<i>Angew. Chem. Int. Ed.</i> 55 , 2697 (2016)
MAF-X27-OH		CO: 7910	<i>J. Am. Chem. Soc.</i> 140 , 38 (2018)
ZIF-67	[Ru(bpy) ₃] ²⁺ /TEOA	CO: 3890	<i>J. Mater. Chem. A</i> 6 , 4768 (2018)
Ni(TPA/TEG)		CO: 15866	<i>Sci. Adv.</i> 3 , e1700921 (2017)
Ni-MOF monolayer		CO: 12500	<i>Angew. Chem. Int. Ed.</i> 57 , 16811 (2018)
Co ₃ O ₄ platelets		CO: 3523	<i>Adv. Mater.</i> 28 , 6485 (2016)
Enzyme/TiO ₂	[Ru(bpy) ₃] ²⁺ /H ₂ O	CO: 300	<i>Energy Environ. Sci.</i> 4 , 2393 (2011)
carbon nitride	Co(bpy) ²⁺ /TEOA	CO: 297	<i>Angew. Chem. Int. Ed.</i> 53 , 11926 (2014)
MOF-525-Co		CO: 202 CH ₄ : 35	<i>Angew. Chem. Int. Ed.</i> 55 , 14310 (2016)
UiO-66/CNNS	N.P. ^a /TEOA	CO: 9.79	<i>Adv. Funct. Mater.</i> 25 , 5360 (2015)

^a N.P.: not applicable.